IL NUOVO CIMENTO Vol. 25 C, N. 4 Luglio-Agosto 2002

Lateral-distribution functions for giant air showers

J. N. Capdevielle([1]), C. Le Gall([1]), J. Gawin([2]), I. Kurp([2]), B. Szabelska([2]) J. Szabelski([2]) and T. Wibig([2])([3])

([1]) *PCC, Collège de France - 11 Pl. M. Berthelot, 75231 Paris Cedex 05, France*
([2]) *The Andrzej Sołtan Institute for Nuclear Studies - 90-950 Łódź 1, Box 447, Poland*
([3]) *Experimental Physics Department, University of Łódź - Pomorska 149/153, Łódź, Poland*

(ricevuto il 24 Aprile 2001; approvato il 20 Febbraio 2002)

Summary. — We have compared the lateral analytical structure functions coming from cascade theory to the numerical distributions generated by EAS Monte Carlo simulations and to the empirical functions used in giant air showers experiments. Introducing the Gaussian hypergeometric formalism, we have improved the analytical description in the most common topological situations and we propose a new function characterized by both terms fitted separately to the electron-positron and the muon components. Important effects in the accuracy of the core position determination are underlined and consequences for the primary energy estimation are discussed. The consecutive treatment and interpretation of the data contained in the catalogues of Volcano Ranch and Yakutsk, completed by the most energetic event of AGASA, are presented. Results might have important implications for detector configuration of the future giant air shower arrays.

PACS 96.40.Pq – Extensive air showers.
PACS 96.40.De – Composition, energy spectra, and interactions.
PACS 13.85.Tp – Cosmic-ray interactions.

1. – Introduction

Four decades ago, in Volcano Ranch array [1] the first extensive air shower recorded above 10^{10} GeV was inaugurating the collection of ultrahigh energy events containing the earliest Giant Air Shower (GAS) with energy estimated around $1.4 \cdot 10^{11}$ GeV. The appearance of an ankle in the primary spectrum at the highest energies was the occasion to appreciate the validity of the question arising from the experimental data: were the particles of extragalactic origin taking over from those of galactic origin? The famous answer [2, 3] came soon, formulated in the so-called Greisen-Zatsepin-Kuzmin (GZK) cutoff, indicating that particles with energy around 10^{11} GeV may interact with photons of the microwave background radiation and could not propagate on very large distances. The evidence of the violation of this cutoff was rising with the number of events detected in the UHE region and the confirmation has become one of the most important challenges

of the new millennium, concerning both astrophysics and high-energy physics, underlined by the emergence of new large instruments, like the Pierre Auger Observatory (PAO) recording EAS on 3000 km^2 [4].

Near vertical showers, detected at such energies, are close to their maximum of development at moderate altitudes (around 1 to 1.5 km) and the conversions from size to primary energy are not too much depending on nuclear interaction models. However, the estimation of the size or any other estimator related to the primary energy E_0, such as densities around 600 to 1000 m from the shower axis, remains a difficult task for arrays where detectors are separated by 1 km or more; a small number of detectors are hit (for statistical reasons, far from axis, with small densities) and the interpolation of densities at significant distances, or the integration performed on axis distance to obtain the total size, depends on the axis determination. About 50% of the particles are contained inside one Molière radius r_{M} (which is about 90–100 m at those altitudes) and 95% remains inside 3.5 r_{M}; it is usually admitted in cascade theory that beyond such distance the scaling with r_{M} fails [5].

The goal of this paper is to weave the role of the topological treatments between theory and experiment, on the one hand, theoretical descriptions coming from the lateral spread theory of electromagnetic cascades, as well as muon lateral-distribution functions and on the other hand, the empirical structure functions for very large distances derived from the compilation of giant EAS measurements. Our approach is organized in sections, as follows: radial distributions of charged particles (sect. **2**); primary energy estimation, consequences of axis position determination (sect. **3**); treatment of UHE existing data (Volcano Ranch, Yakutsk, AGASA) (sect. **4**).

This elementary step concerns only the experiments dealing with scintillators, registering charged particles in the most simple conditions, as a preliminary work before entering upon different situations of water Cherenkov detectors, like in Haverah Park array [6] or in PAO, as well as the detection of the fluorescent component [7].

2. – The lateral distribution of charged particles

2˙1. *Radial electron distribution from cascade theory.* – The structure functions $f(x)$ in 3-dimensional cascade theory (where $x = r/r_{\mathrm{M}}$, r being the distance to the core in meters), generally normalized so that $\int_0^\infty 2\pi x f(x)\mathrm{d}x = 1$, are related to the electron density $\Delta_{\mathrm{e}}(r)$ by $\Delta_{\mathrm{e}}(r) = N_{\mathrm{e}} f(x)/r_{\mathrm{M}}^2$. The analytical parameterizations of numerical results from the solutions of diffusion equations or from Monte Carlo calculations are commonly classified following the earliest proposed forms:

$$f(x) = 0.45(1/x + 4)\exp[-4x^{2/3}], \tag{1}$$

$$= c(s)x^{s-2}(x+1)^{s-4.5}, \tag{2}$$

$$= g(s)x^{s-a}(x+1)^{s-b}(1 + d\cdot x)^{-c}. \tag{3}$$

The former approximation (eq. (1)), as quoted by Williams [8], was derived by Bethe from Molière's theory for small values of the argument x and for $s = 1$; this form was generalized by Nishimura and Kamata following the numerical values of their solutions of transport equations via Mellin's and Hankel's transformations in the complex plane and saddle point approximation to get the final real solutions [9]. The synthesis, the so-called NKG formula [10], contained in eq. (2) under a pair of power laws representing respectively the asymptotic tendencies (near and far from the shower core), with a simple

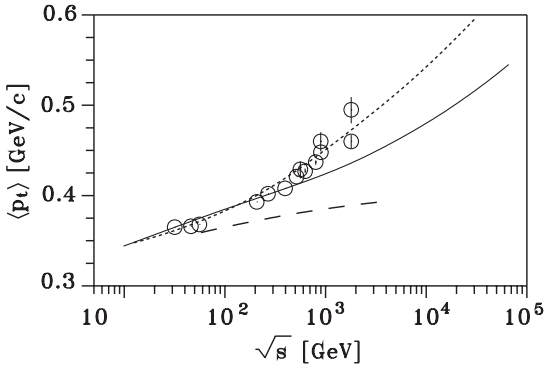

Fig. 1. – Dependence of p_{t} *vs.* $\sqrt{(}s)$. The collider data (○) is plotted together with CORSIKA options, original HDPM (solid line), Venus model (dashed line), HDPM modified following UA1-MIMI 96 data (dotted line).

normalization in terms of the Euler beta-function,

$$c(s) = \frac{\Gamma(4.5 - s)}{2\pi\Gamma(s)\Gamma(4.5 - 2s)}, \tag{4}$$

became one of the most widely used radial distributions. The comparison to experimental results suggested however a more complex situation and some corrections such as the introduction of a new argument $x = r/kr_{\mathrm{M}}$, k being a factor reducing Molière radius, or a local age parameter $s(r)$, troublesome for the normalization of the structure function [11, 12]. In order to provide a better skewness than the transition between two power laws, we proposed later [13] the more complex relation of eq. (3); such structure function, which is also a general form containing eq. (2) for a particular set of parameters, has the advantage (for values of parameters respecting the conditions of convergence $s-a+2 > 0$ and $c-2s+b-2 > 0$) to be exactly normalized in terms of the Gaussian hypergeometric function $F_{\mathrm{HG}} = F(c, s - a + 2, c + b - s; 1 - d)$ by

$$g(s) = \frac{\Gamma(c + b - s)}{2\pi\Gamma(s - a + 2)\Gamma(c - 2s + b + a - 2)F_{\mathrm{HG}}}. \tag{5}$$

At large distances from the axis, as emphasized by the Particle Data Group [5], the description of the 3D-cascade transport by diffusion equations fails (small-angle approximation in multiple Coulomb scattering, effect of single scattering, Landau approximation is no more valid) and the analytical descriptions can be derived only from Monte Carlo or semi Monte Carlo calculations [14] in order to restore some useful scaling properties. For instance, the condition $|\ln(E_\gamma/\varepsilon)| \gg |\ln(r/r_{\mathrm{M}})|$, where E_γ is the primary photon energy and ε the energy threshold for electrons, is no more fulfilled for a large number of subcascades in giant EAS at very large distance from the shower axis, a circumstance where both Approximation B and Landau's Approximation [15] are no more valid.

2˙2. *Characteristics of lateral spread in GAS.* – In pure e.m. cascade, even at the highest energies, we can describe the radial distributions as consequences of multiple- and single-electron scattering; the 3-dimensional development of the e.m. component in

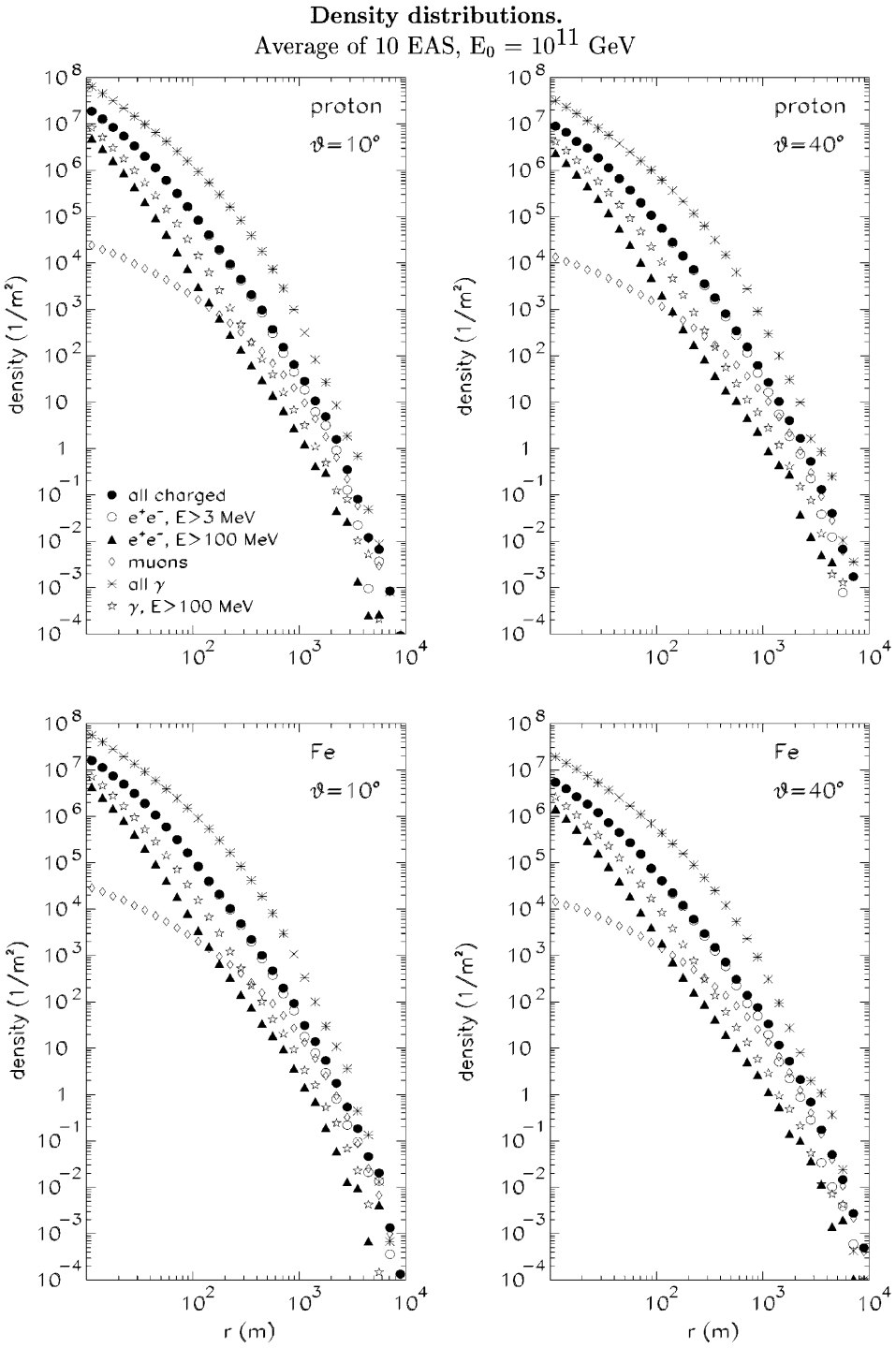

Fig. 2. – Lateral density distribution for several components of EAS for proton and iron primary particles with energy 10^{11} GeV and zenith angle 10° and 40°, as indicated.

GAS reflects in addition the effects of other agents, such as the transverse-momentum distribution and the geomagnetic field. Some models suggest that the average transverse momentum p_{t} in the earliest interactions can be close to 1 GeV/c, and even larger in individual collisions of large multiplicity, because of the correlation betwen $\langle p_{\mathrm{t}} \rangle$ and the central rapidity density $\mathrm{d}n/\mathrm{d}y$ [16, 17]. The consequences of the energy rise of $\langle p_{\mathrm{t}} \rangle$ (fig. 1) on the lateral muon and hadron distributions cannot be disregarded. The muons generated at high altitude are submitted to the geomagnetic field during a long trajectory, and for inclined showers the muon development suffers some distortion from the traditional cylindrical symmetry, as shown by simulations with CORSIKA [18, 19] after separation of positive and negative muons [20]. Just to illustrate the complexity of the lateral distributions very far from the axis, we have plotted in fig. 2 the lateral distributions obtained for photons, electrons and muons at distances from 10 m up to 10 km, averaged for 10 initiated showers ($E_0 = 10^{11}$ GeV, CORSIKA with thinning factor 10^{-6}) for zenith angles $\theta = 10^\circ$ and 40°. All those showers have been simulated with the Quark Gluon String Model [21]; the respective energy thresholds are here 3 MeV for electrons and photons and 300 MeV for muons.

2˙3. *Empirical distributions for giant EAS .* – The empirical structure functions were inspired by the theoretical functions quoted in sect. **2**; as fitted to scintillator experiments, they deal generally with densities of charged particles $\varrho(r)$ (and not with pure electrons). We will refer to the following functions used for GAS: AGASA #1, AGASA #2, Akeno, Linsley's function and Yakutsk function for electrons. They are described in details in appendix A. The muon component contribution to the total charged-particle density is significant at large distances from the core. It is interesting to observe that beyond 1.5 km the lateral distribution profile for charged particles turns to be dominated by muons. However, if conditions put an energy limit for electromagnetic components, then muons can dominate much nearer to the core (*e.g.*, near 200 m for electromagnetic energy threshold 100 MeV, as presented in fig. 2). Details of some muon lateral-distribution functions can be found in appendix B.

3. – The inverse problem

3˙1. *The conversion to primary energy near maximum.* – At altitudes around 1000 m above sea level, near vertical showers of energy 10^{10-11} GeV are close to the maximum of their longitudinal development; this favourable circumstance reduces the model dependence, and as far as the cascade curve is more flat around the maximum, the fluctuations are reduced as well as the discrepancies between primary protons and heavy nuclei. This advantage disappears for inclined showers where the dependence on nuclear interaction models and on fluctuations can no more be neglected. The distortion of γ-induced showers by the LPM effect, quite more important than for primary protons in this energy range raises also problems in the primary energy evaluation. The rule of thumb from cascade theory that there is a simple proportionality between primary energy and total size near the maximum can be used here as a first approximation in the approach of the total primary energy estimation. For instance, in Volcano Ranch [1], the primary particle energy E_{CR} is determined in the following way: $E_{\mathrm{CR}} = 10^9 \cdot N_{\mathrm{V}} \cdot (20 - 3.3u + 0.15u^2)$ eV, where $u = \log(N_{\mathrm{V}})$, $N_{\mathrm{V}} = N_{\mathrm{e}} \cdot \exp\left[\frac{x-x_0}{\lambda}\right]$ and (for Volcano Ranch) $x_0 = 834$ g/ cm^2, $x = x_0 \cdot \sec\theta$, $\lambda = 300$ g/cm^2. In AGASA [22], as well as in Yakutsk [23], the respective densities at 600 m are directly converted to primary energy (in eV), also by a

quasi-proportionality:

$$E_0 = (2.03 \pm 0.1) \cdot 10^{17} S_0(600)^{1.02\pm0.02}, \tag{6}$$

$$= (4.6 \pm 1.2) \cdot 10^{17} \varrho_0(600)^{0.96\pm0.03}; \tag{7}$$

$S(600)$ is here the total density recorded by plastic scintillators in AGASA. The conversion to primary energy for inclined showers is still dominated by the absorption resulting from simulations involving interaction models being in fashion during the construction of the different arrays.

Similarly to Volcano Ranch for total size, the absorption is parameterized for the densities at 600 m, for AGASA and Yakutsk, respectively,

$$S_0(600) = S_\theta(600) \cdot \exp\left[\frac{X_0}{500} \cdot (\sec\theta - 1) + \frac{X_0}{594} \cdot (\sec\theta - 1)^2\right],$$

$$\varrho_0(600) = \varrho_\theta(600) \exp\left[\frac{X_0}{500} \cdot (\sec\theta - 1)\right]. \tag{8}$$

The vertical depth X_0 is taken as 920 g/cm^2 for AGASA and 1020 g/cm^2 for Yakutsk (where $\theta \leq 60°$). After integration of eq. (B.5), the total number of muons in Yakutsk can be used for the conversion to primary energy, according to

$$N_\mu = 2\pi \cdot K(\theta) \cdot r_0^2 \cdot \left(\frac{E_0}{10^{18}\ \mathrm{eV}}\right)^{0.87} \cdot \frac{\Gamma(1.25) \cdot \Gamma(b_\mu - 2)}{\Gamma(b_\mu - 0.75)},$$

where $r_0 = 280$ m, $K(\theta) = 13.3 \cdot \exp\left[\left(\frac{1}{\cos\theta} - 1\right) \cdot \frac{1020}{440}\right]$, $b_\mu = b_0 + b_1 \cos\theta + b_2(\log E_0 - 18)$, $b_0 = 0.98 \pm 0.03$, $b_1 = 2.28 \pm 0.3$, $b_2 = 0.09 \pm 0.01$. In 1991, after the evaluation of the total primary energy through the energy carried by secondary particles and from the Cherenkov component, the conversion relation (7) in Yakutsk was slightly changed as

$$E_0 = (4.8 \pm 1.0) \cdot 10^{17} \varrho_0\,(600)^{1.0\pm0.02} \tag{9}$$

for a temperature of $-40°$C [24].

In the special situation of SUGAR array [25], based on the detection of the penetrating component, one function similar to eq. (B.2) is used for muon densities, including zenith angle dependence, $r_0 = 320$ m, $\alpha_1 = 0.75$ and $\beta_1 = 1.50 + 1.86\cos\theta$. The normalization is obtained through

$$C_\mu = K(\theta) = \frac{\Gamma(\beta_1)}{2\pi\Gamma(2 - \alpha_1)\Gamma(\alpha_1 + \beta_1 - 2)}.$$

The total muon size $N_\mu(\theta)$ is then converted to the vertical muon size $N_{\mu\mathrm{v}}$ and the primary energy is derived (in eV) as

$$E_0 = 1.64 \cdot 10^{18} \left(\frac{N_{\mu\mathrm{v}}}{10^7}\right)^{1.075}. \tag{10}$$

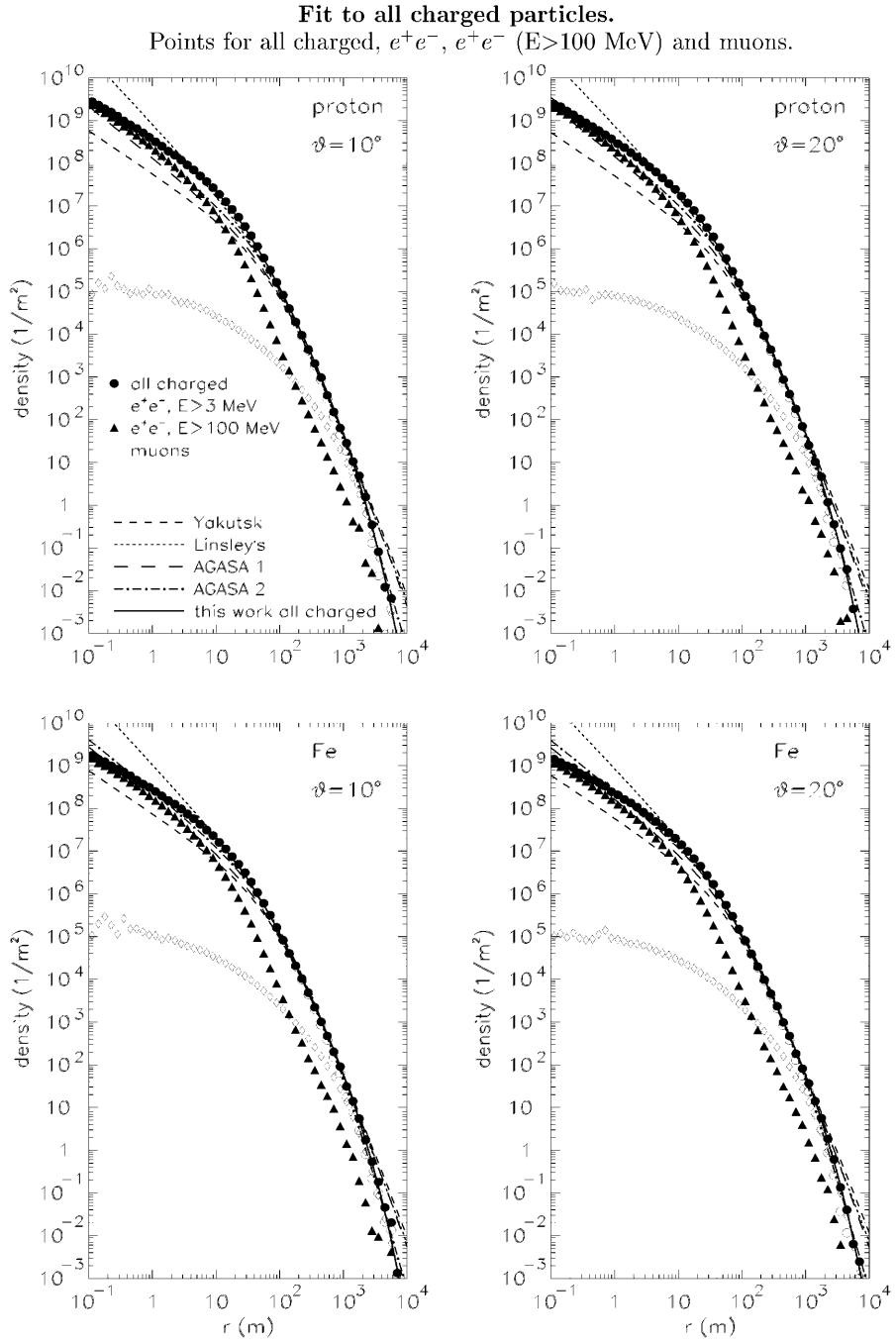

Fig. 3. – Fits to all charged particles lateral distribution from simulations (average from 10 EAS). Primary particle energy 10^{11} GeV. Lines are normalized to $\varrho(600\text{ m})$. See table I for comparison of N_e and other parameters of different functions. For solid line (this work) see formula (11) and parameters from table II.

TABLE I. – *N_e and some parameters for fits presented in fig. 3. In the top row the primary particle and the zenith angle are indicated. Columns a present total number of charged particles N_e in 10^{10}, columns b the ratios E_0/N_e in GeV ($E_0 = 10^{11}$) GeV and columns c the ratios $\varrho(600)/N_e$ in 10^{-8} particles/m^2. N_e for "this work" correspond to average sizes of 10 simulated EAS. $m(600) = \frac{d(\log \varrho)}{d(\log r)}$ at 600 m. Owing to more precise adjustment at short distances (< 200 m in fig. 3), where the majority of particles are contained, only the function JNC can restore the size.*

	proton 10°	proton 20°	iron 10°	iron 20°
$\varrho(600)$	290 m^{-2}	318 m^{-2}	369 m^{-2}	356 m^{-2}
$E_0/\varrho(600)$ (GeV m^2)	$3.4 \cdot 10^8$	$3.1 \cdot 10^8$	$2.7 \cdot 10^8$	$2.8 \cdot 10^8$
$m(600)$	–3.9	–3.6	–3.6	–4.0

fit	1*a*	1*b*	1*c*	2*a*	2*b*	2*c*	3*a*	3*b*	3*c*	4*a*	4*b*	4*c*
Yakutsk	1.8	5.6	1.6	1.7	5.9	1.9	2.3	4.3	1.6	1.9	5.3	1.8
Linsley's	8.2	1.2	0.3	8.0	1.3	0.3	10.5	0.9	0.3	8.9	1.1	0.4
AGASA #1	2.4	4.2	1.2	2.6	3.8	1.2	3.1	3.2	1.1	2.9	3.4	1.2
AGASA #2	3.3	3.0	0.8	3.6	2.8	0.8	4.2	2.4	0.8	4.0	2.5	0.8
this work	5.6	1.8	0.5	5.6	1.9	0.6	5.1	2.0	0.7	4.5	2.2	0.7

3˙2. *The approach of ϱ_{600} and other estimators* . – As far as one density at a particular distance is considered as a good estimator of primary energy, the determination (here at 600 m) of the densities in the neighbourhood becomes crucial to perform an accurate interpolation at 600 m (in the best circumstance, where this distance is "contained" between measured densities). In the case of detectors separated by large distances, 1.5 km or more, there can be situations where the density can be only extrapolated to lower distances from groups of densities measured only above 800 m. The interpolation of the density (and the extrapolation if necessary) can be more safe, when the analytic properties of cascade theory can be restored from the total sample of measured density;

TABLE II. – *Best parameters to simulated e^+e^-+ muons (all charged) lateral-distribution fit using JNC01 formula* (11). *Labels p10, p20, Fe10 and Fe20 in the first row refer to primary particle (proton or iron) and to the zenith angle* (10° *or* 20°).

	p10	p20	Fe10	Fe20
$\log N_e$	10.75	10.72	10.70	10.65
r_M	21.26	21.26	19.18	19.18
r_0	8785.	8785.	9536.	9536.
a	1.91	1.91	1.82	1.82
s	1.03	1.04	1.03	1.04
b	3.32	3.32	3.31	3.31
β	10.0	10.0	10.0	10.0

this coherence can help when using the Akeno function (eq. (A.5)) containing the age parameter for large air showers up to 3–4 Molière radii by distinguishing the "old" or "young" aspect of each shower. In the case of GAS, we notice in fig. 2 that in all cases the lateral muon densities become dominant for $r \geq 1.5$ km ($r \geq 200$ m for electrons with $E > 100$ MeV) in the lateral distribution of charged particles; the lateral muon distribution flattens for showers initiated at higher altitude, just when the lateral electron distribution corresponds also to older profile. This circumstance, and the opposite situation for showers initiated deeper in the atmosphere, suggest the extension of the concept of lateral age parameter to the total lateral charged-particles distribution of GAS, using the skewness of the profiles described by our Gaussian hypergeometric distribution (eq. (3)); the parameters have been adjusted with MINUIT from our Monte Carlo simulation, giving the JNC functions

$$\varrho(r) = N_{\mathrm{e}} \cdot C \cdot x^{-\alpha} \cdot (1+x)^{(\alpha-\eta)} \cdot (1+d\cdot x)^{-\beta}, \tag{11}$$

where $x = r/r_{\mathrm{M}},\ d = r_{\mathrm{M}}/r_0,\ s = 1.03,\ \alpha = a - s,\ \eta = b - s + \alpha,$

$$C = \frac{1}{2\pi \cdot r_{\mathrm{M}}^2} \cdot \frac{\Gamma(\beta+\eta-\alpha)}{\Gamma(2-\alpha)\cdot\Gamma(\beta+\eta-2)} \cdot \frac{1}{F_{\mathrm{HG}}(\beta, 2-\alpha; \beta+\eta-\alpha; 1-d)}$$

with the conditions $2-\alpha > 0$ and $\beta+\eta-2 > 0$. The hypergeometrical function (F_{HG}) is defined in appendix A (subsect. A˙1, eq. (A.3)).

We will consider 4 different lateral distributions in the form of eq. (11):

– JNC01 (solid lines in fig. 3 and parameters from table II) is the description of all charged particle densities (s parameter dependence is presented in the top fig. 4),

– JNC02 (solid lines in fig. 5 and table III) represents $\mathrm{e}^+ + \mathrm{e}^-$ densities only (s parameter dependence—in the bottom fig. 4),

– JNC03 is the sum of JNC02 and muon lateral distribution (formula (B.2) with parameters from table V) (our favorite description for scintillator detector data),

– JNC04 for $\mathrm{e}^+ + \mathrm{e}^-$ with $E > 100$ MeV (solid lines in fig. 6 and parameters from table IV).

It will be seen in sect. **4** (where the set of coefficients is reproduced in table II) that this distribution containing a modulation via the extended s gives better χ^2 values to determine $\varrho(600)$ and that a special procedure can help the total size estimations. This procedure consists of adjusting separately the electron and muon densities to receive a correct convergence to the electron and muons sizes, N_{e} and N_μ, respectively (in circumstances, where a larger number of densities are recorded very far from the axis, there is a risk of tendency to converge to N_μ rather than to N_{e}). For this purpose we shall distinguish the function JNC02 (restricted to electrons), also given by relation (11), with the set of parameters reproduced in table III (sect. **4**). Another primary energy estimator could be the couple $(\varrho(600), s)$, with the correlation [26] in quadratic form $E_0/\varrho(600) = a(s-1)^2 + b$ that we have proposed.

An underlying fundamental condition for a correct estimation is also an accurate axis determination. From fig. 3 we notice the linear dependence $\log(\varrho)$ *vs.* $\log(r)$ near 600 m. Therefore $\Delta\varrho/\varrho = m(600)\cdot\Delta r/r$ (where $m(600)$ is in table I), and 60 m (10%) accuracy in determining the core position corresponds to about 40% error in $\varrho(600)$ determination.

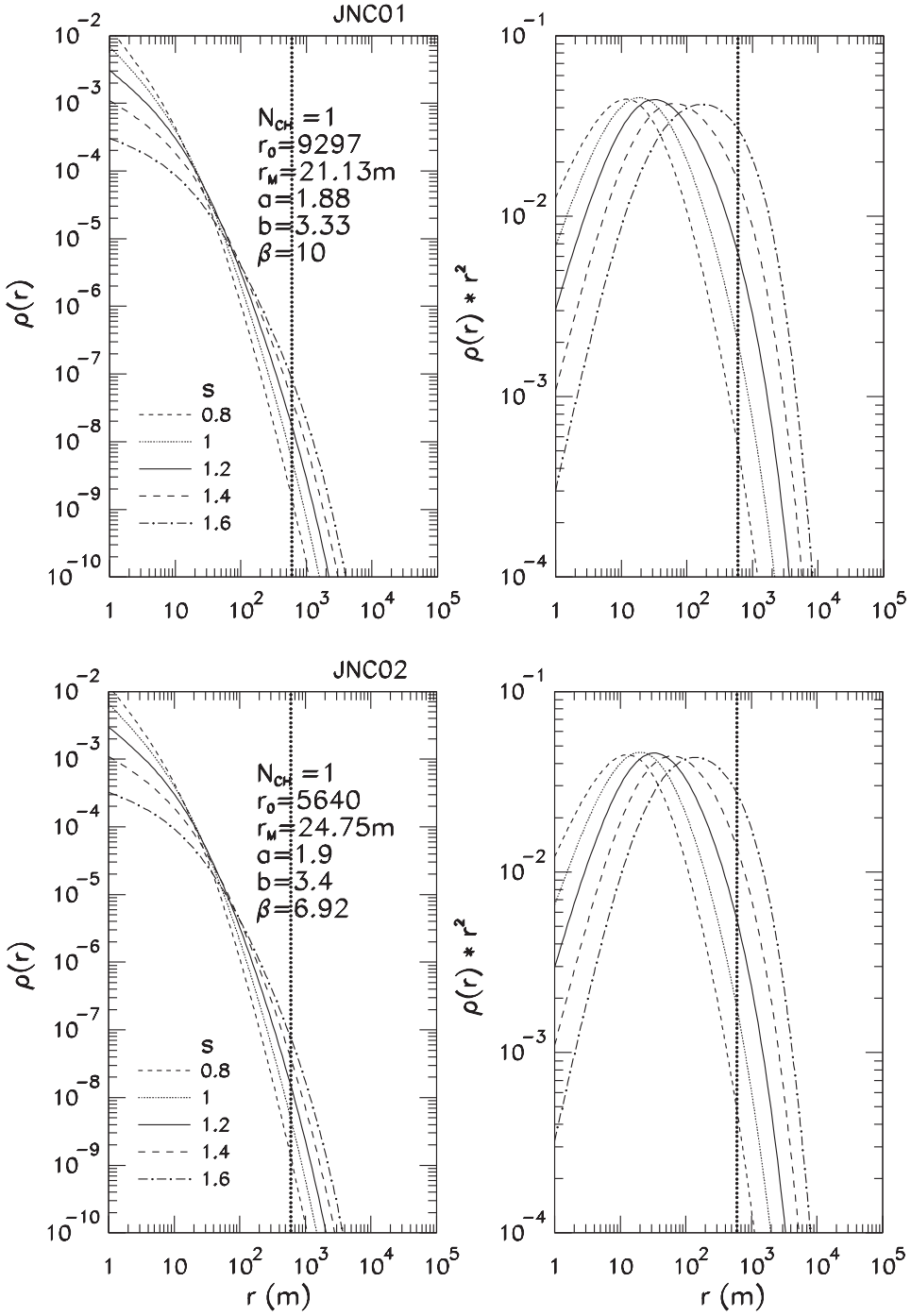

Fig. 4. – Top: distribution of all charged particles with JNC01 function (see formula 11 and table II). Bottom: JNC02 function for e^+e^- (see formula (11) and table III).

TABLE III. – *Best parameters to e^+e^- ($E > 3$ MeV) lateral-distribution fit using JNC02 formula* (11).

	p10	p20	Fe10	Fe20
$\log N_e$	10.75	10.72	10.71	10.65
r_M	20.65	20.65	28.48	28.48
r_0	2698.	2698.	11423	11423
a	1.91	1.91	1.86	1.86
s	1.03	1.05	1.03	1.02
b	3.22	3.22	3.63	3.63
β	5.82	5.82	10.0	10.0

3˙3. *Axis determination* . – The core position has been obtained by minimization with Minuit program between different formulas available for lateral densities written *vs.* the coordinates X, Y as

$$\varrho(r) = \varrho(\sqrt{(X - X_c)^2 + (Y - Y_c)^2}), \tag{12}$$

where the core coordinates X_c and Y_c are taken as two additive parameters in the minimization. We pointed out from the simulation that the barycenter was separated in average by about 180 m from the actual core (for a sparse array with a grid of 1.5 km [26]). We use the barycenter position as initial values for the parameters X_c and Y_c. The procedure has been tested on simulated showers, as well as on the catalogues of Volcano Ranch and Yakutsk experiments, by the optimization on size, core position and other free parameters (*i.e.* age s).

As will be discussed in sect. **4**, the core position obtained depends on the profile of the structure function chosen which can be more or less adequate to the natural lateral charged-particle distribution.

3˙4. *Adjustment to simulated lateral distributions*. – In order to appreciate the advantages of the hypergeometric Gaussian approach compared to the classical Eulerian description, we have fitted for example the average radial distributions derived from groups of 10 showers simulated with CORSIKA for $E_0 = 10^{20}$ eV, for zenith angles 10° and 20°, respectively, for protons and iron nuclei primaries. In each case, the adjustment has been performed with 50 points from the simulation distributed from 0.1 m up to 10 km from axis position for charged particles (muons and electrons) as shown in fig. 3. It appears that at distances lower than 200 m only the hypergeometric approach by reason of its skewness provides a correct adjustment, when systematically Linsley's function (eq. (A.6)) overestimates the densities and Yakutsk (eq. (A.7)) or AGASA (eqs. (A.1) and (A.4)) functions underestimate the densities; the consequence (table I), as a majority of particles are contained in this area, is that the JNC function is the only one suitable to recover the size.

This operation was repeated separately for electrons ($E > 3$ MeV) (using the JNC02 function, the same form as JNC01, with different parameter values listed in table III) (see fig. 5), for electrons ($E > 100$ MeV) (JNC04 function, parameters in table IV) (fig. 6), and muons (fig. 7) using the function given in relation (B.2) and parameters from table V.

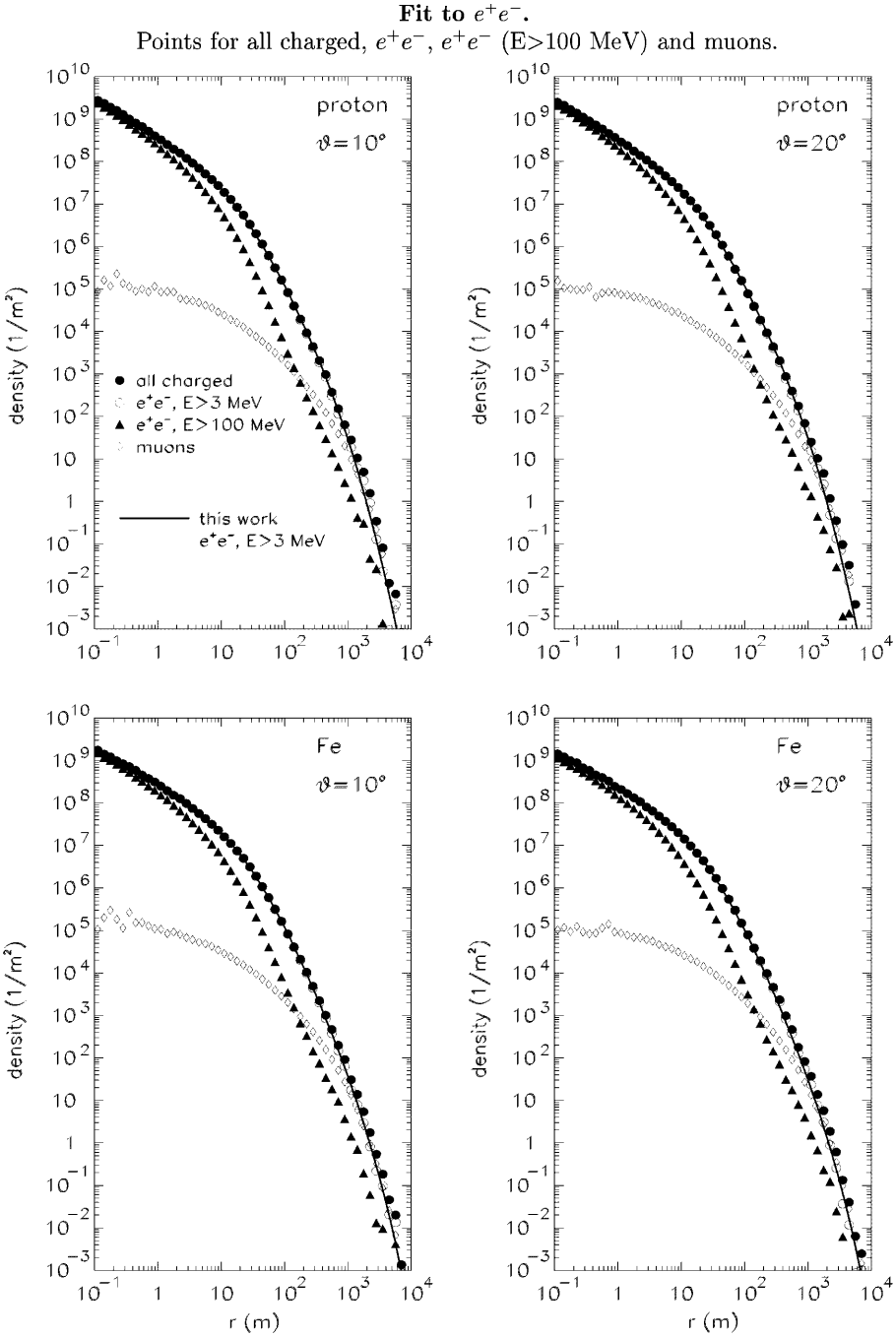

Fig. 5. – Fits to electrons and positrons ($E > 3$ MeV) using formula (11) and parameters from table III.

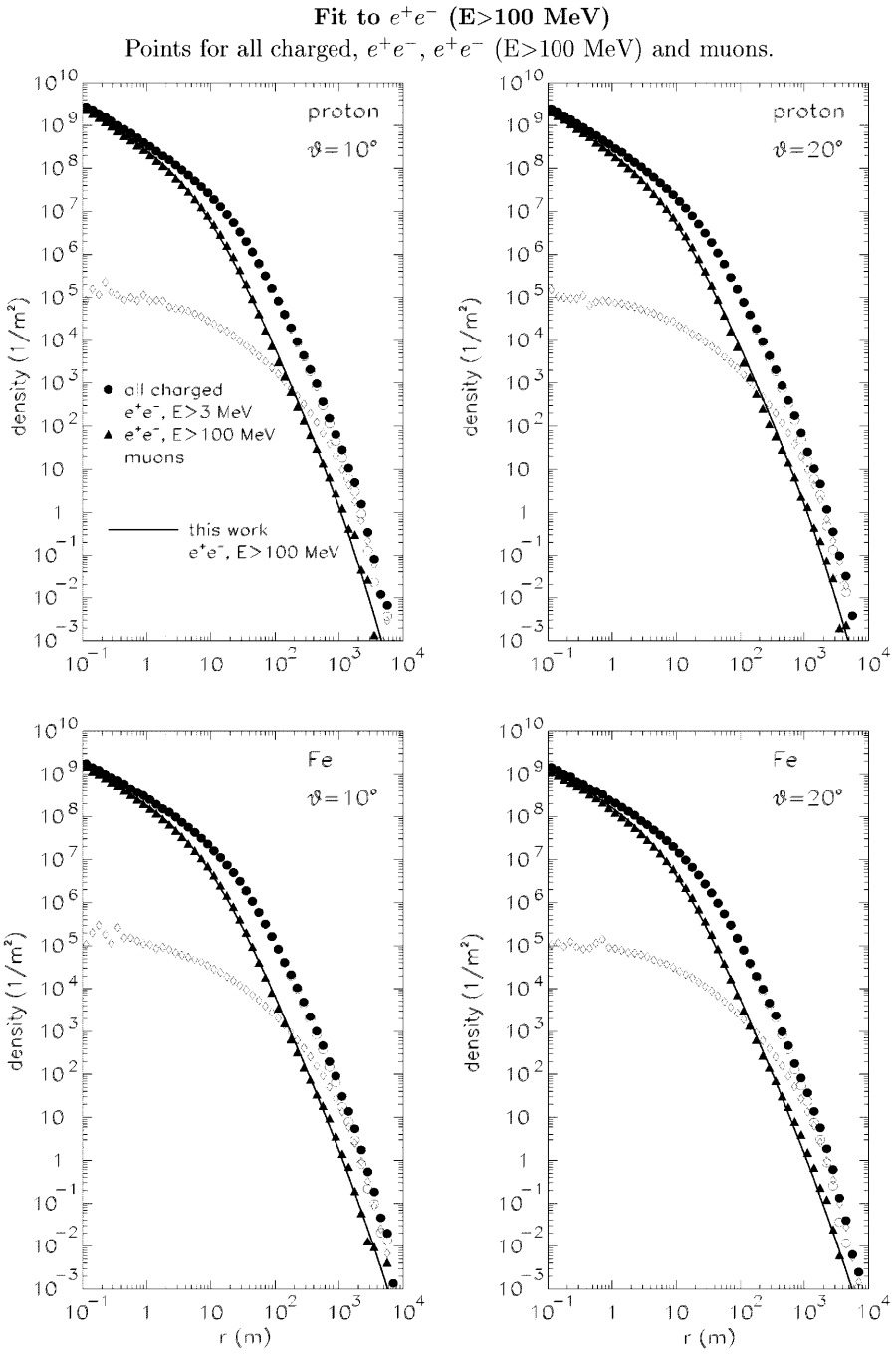

Fig. 6. – Fits to electrons and positrons ($E >$ 100 MeV) using formula (11) and parameters from table IV.

TABLE IV. – *Best parameters to e^+e^- ($E > 100$ MeV) lateral-distribution fit using JNC04 formula* (11).

	p10	p20	Fe10	Fe20
$\log N_e$	10.11	10.07	10.04	9.97
r_M	7.52	7.52	9.05	9.05
r_0	3472.	3472.	4202.	4202.
a	1.88	1.88	1.85	1.85
s	1.03	1.05	1.03	1.03
b	3.62	3.62	3.73	3.73
β	3.31	3.31	2.00	2.00

We have just explored some combinations of parameters included in intervals of values currently used in the experimental data and this does not exclude that best sets of parameters could be obtained with different initializations (for instance starting with one Moliére radius reduced artificially divided by 3).

The fitting procedure was carried using MINUIT and we have added for the numerical evaluation of the quality of the adjustment the factor

$$\chi^2_f(50) = \sum_{i=1}^{50} \frac{(Y_i - F_i)^2}{Y_i}, \tag{13}$$

where $Y_i = \varrho(r_i)$ for the simulated average value, and $F_i = \varrho(r_i)$ for the value evaluated from the fit formula.

An acceptable agreement is obtained for the muon densities (fig. 7) with the Euler beta-function (formula (B.2)); however, the situation could be improved, herealso, with a hypergeometric description.

4. – Treatment of Volcano Ranch, Yakutsk and Akeno data

4˙1. *Method of localization.* – We assume that the directions of registered showers were determined sufficiently accurate by analyzing timing from many detectors. However estimation of $\varrho(600)$ or N_e depends on the form of the lateral-distribution function used to fit the registered number of particles and on localization methods (*i.e.* the form of the function chosen for minimization).

TABLE V. – *Best parameters to simulated muon lateral-distribution fit using formula* (B.2) *(see fig.* 7*).*

	p10	p20	Fe10	Fe20
$\log N_\mu$	8.76	8.74	8.87	8.85
r_0	1098.	766.	867.	741.
α_1	0.56	0.54	0.55	0.50
β_1	7.04	5.65	6.04	5.60

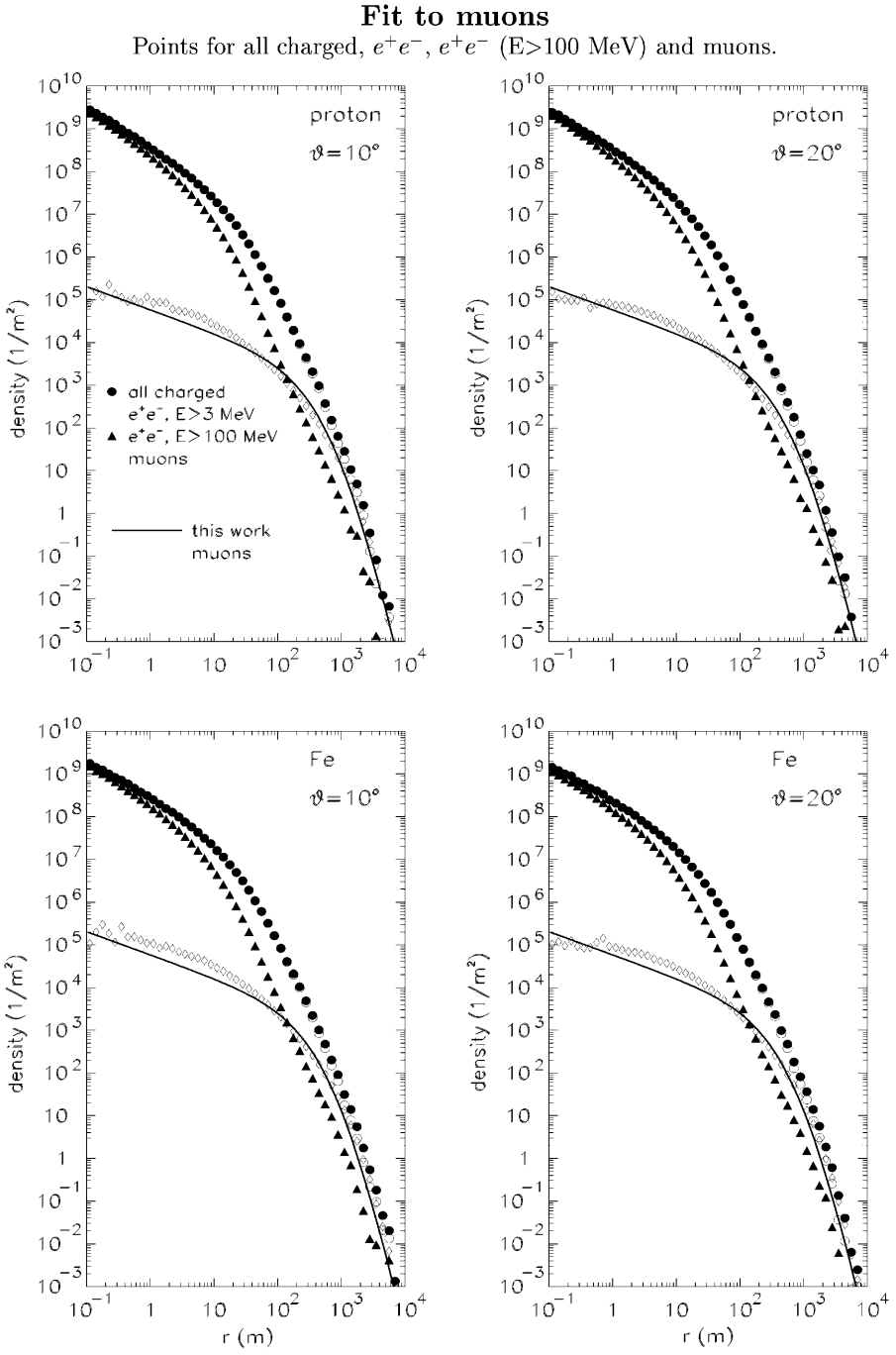

Fig. 7. – Fits to muons using formula (B.2) and parameters from table V.

We have used 6 fits to the charged-particle lateral distribution:

A) The JNC01 function for all charged particles (eq. (11) and top fig. 4). The free parameters are x, y, $N_{\rm e}$ and s. We take the average values for other parameters: $r_{\rm M} = 21.13$ m, $r_0 = 9297$ m, $a = 1.88$, $b = 3.33$, $\beta = 10$.

B) The JNC03 function as the sum of JNC02 function for e^+e^- (eq. (11) and bottom fig. 4) and function for muons (eq. (B.2)). The free parameters are x, y, $N_{\rm e}$ and s. We take $N_\mu = 0.05 \cdot N_{\rm e}$. We take the average values for JNC02 parameters: $r_{\rm M} = 24.75$ m, $r_0 = 5640$ m, $a = 1.9$, $b = 3.4$, $\beta = 6.92$.

C) Yakutsk function (see subsect. A˙5). The free parameters are x, y and ϱ_{600}.

D) Linsley's function (see subsect. A˙4). The free parameters are x, y and $N_{\rm e}$.

E) AGASA function no. 1 (see subsect. A˙1). Free parameters are x, y and $N_{\rm e}$.

F) AGASA function no. 2 (see subsect. A˙2). Free parameters are x, y and $N_{\rm e}$.

The localizations are performed with MINUIT, taking the minimization of the function

$$\chi^2 = \sum \mathcal{W}(D_i, E_i, F_i, K_i, S_i), \tag{14}$$

where D_i is the number of particles in the i-th detector for the registered event, and $F_i = \varrho(r_i) \cdot A_i$ is the density evaluated from the fit formula multiplied by the A_i—the area of the i-th detector multiplied by $\cos\theta$, θ is the EAS zenith angle, E_i is the estimated accuracy of determination of number of particles, K_i the density level when cascading processes might significantly increase the estimated particle number and S_i is the particle density corresponding to the phototube-ADC saturation level.

When D_i is greater than $K_i \cdot A_i$ and F_i is less than D_i, then $\mathcal{W} = 0$ (the possible cascading process might produce a larger signal); when $\varrho(r_i)$ is larger than S_i, then $\mathcal{W} = 0$ (the expected density is larger than the saturation level); otherwise

$$\mathcal{W}(D_i, E_i, F_i, K_i, S_i) = \frac{(D_i - F_i)^2}{E_i^2},$$

$$E_i = \max\left(\kappa \cdot D_i, \sqrt{D_i}\right),$$

where κ is equal to 0.15 for Volcano Ranch and Yakutsk arrays and 0.10 for AGASA. We put cascading level K_i equal to 200 particles/m^2. In this way we introduce a special treatment of high-density registration. Detectors registering high particle density are very important for estimation of the shape of lateral distribution of particles, as they are relatively near to the EAS core.

The examples of localizations of particular events are presented in appendix C.

4˙2. *Volcano Ranch data.* – The data contained in the catalogue of Volcano Ranch registration [1] was then analyzed event per event: the same localization procedure is first carried with the original function used in the experiment and then repeated with JNC01 and JNC03 functions, and the functions used in another experiments.

The results of our localization procedure are compared in fig. 8 with the original results as given in experimental paper or recalculated by us using Linsley's function of lateral

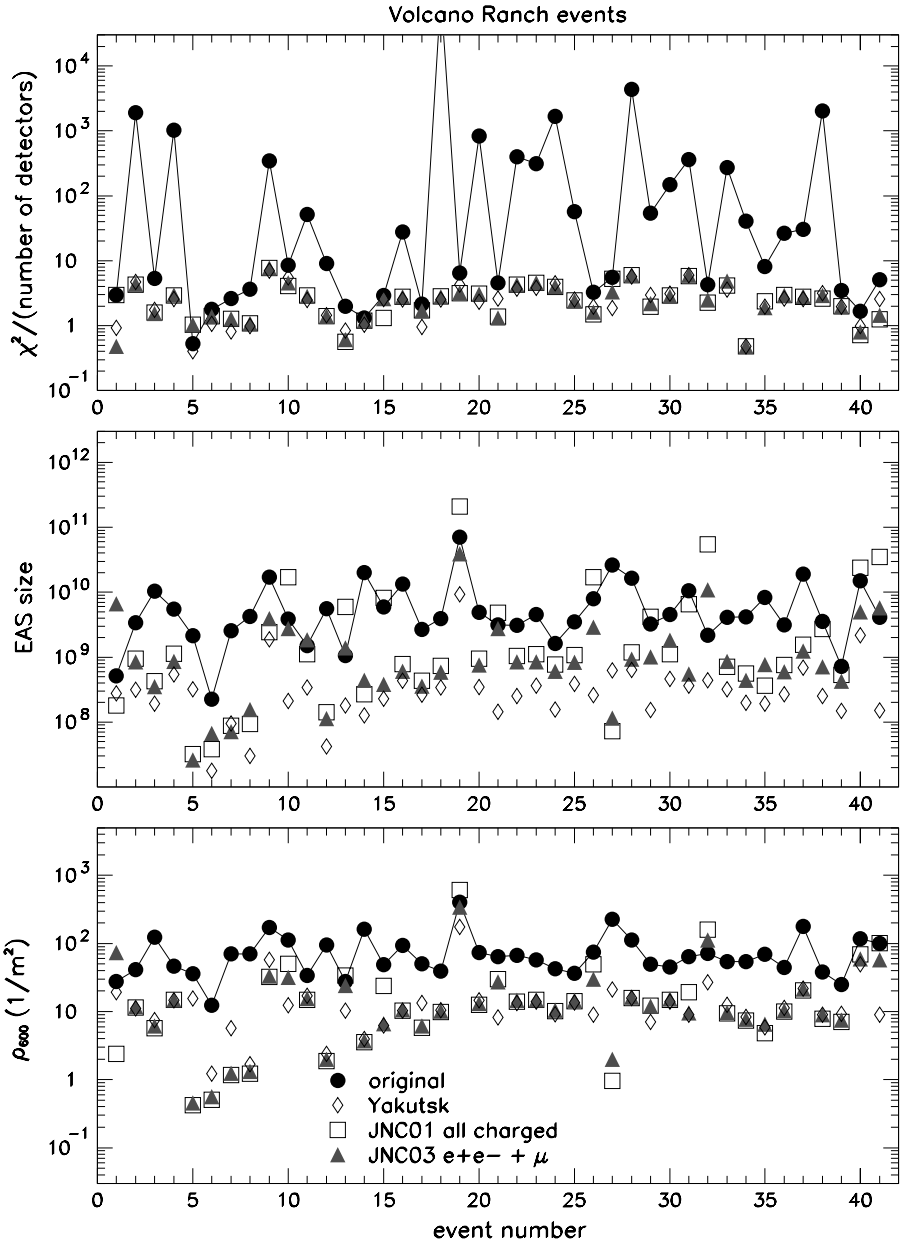

Fig. 8. – Comparison of localization results for Volcano Ranch data. Original results are compared with fits A, B and C.

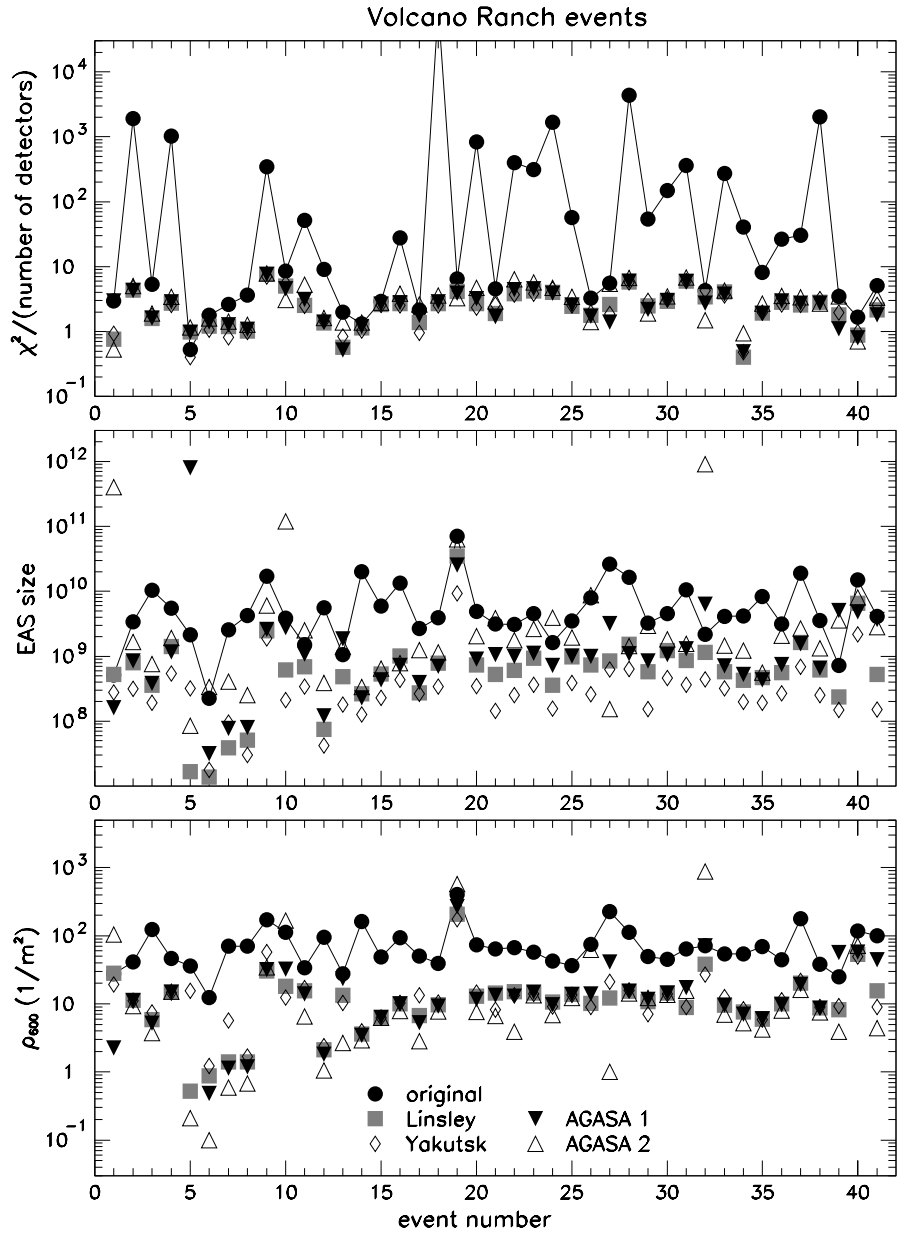

Fig. 9. – Comparison of localization results for Volcano Ranch data. Original results are compared with fits C, D, E and F.

TABLE VI. – *Results of localization for the most energetic AGASA event* [27]*:* χ^2*,* $\varrho(600)$*,* N_e *and relative core distance from the original localization. The comparison is made for different lateral-distribution functions. Age parameter* s *fitted for A and B functions is equal to 0.93 and 0.95, respectively.* Δr *is the distance from the original localization* $(-1150.0, -1350.0)$*.* $\Delta\mathcal{R}$*—distance from the centre for all functions* $(-1264.0, -1348.3)$*.*

	$\chi^2/23$	$\varrho(600)$ $(1/m^2)$	N_e (10^{10})	Δr (m)	$\Delta\mathcal{R}$ (m)
Original	?	892	7.84	0.0	114.0
A – JNC01	4.99	581	16.49	78.1	47.6
B – JNC03	5.03	474	5.05	83.8	30.3
C – Yakutsk	7.73	291	1.47	172.3	61.2
D – Linsley's	7.07	350	6.08	144.1	35.6
E – AGASA no. 1	6.20	431	4.67	112.6	15.3
F – AGASA no. 2	5.24	632	9.23	66.8	61.2

distribution (see subsect. A˙4 and fig. 13). The optimization of the localization and the employment of the new functions turns to one general improvement of the minimization; a better control of the convergence is obtained for JNC functions for all charged particles and for the Yakutsk function (fig. 8 and 9). From the sizes resulting or from the densities interpolated at 600 m, it can be seen that the primary energy originally estimated is reduced in the case of the Yakutsk function by factor ~ 3 and enlarged in the case of the JNC01 function. The very large sizes obtained correspond to hopeless situations where the information is too poor for a rigorous adjustment, *i.e.* 5 or less detectors hit and axis not contained in the array. In the case of the event 19 (considered originally as the first event above 10^{20} eV), the previous estimation of energy would be reduced by about a factor of 2 for both approaches via $\varrho(600)$ or N_e and JNC functions.

4˙3. *Yakutsk data.* – The same treatment has been applied to the showers reported in the catalogue of Yakutsk [23]. The original minimization is here carried with the Yakutsk function. Also for Yakutsk data better minimization is obtained and we observe here that $\varrho(600)$ is generally the same for JNC01 and Yakutsk functions (figs. 10, 11), but size estimations differ by more than one order of magnitude. Still the Yakutsk function provides the smallest sizes, in which case a satisfying agreement with GZK cutoff is also ascertained. However, as we have seen in table I that the actual size was systematically reduced by a factor 3 for the Yakutsk function, this agreement can be only apparent.

4˙4. *Akeno AGASA data.* – In the absence of the catalogue published for Akeno and AGASA data, we were constrained to apply our procedure to the unique and most energetic event of AGASA for which densities and the respective detectors positions are available [27]. The results of the fit are given in table VI. The $\varrho(600)$ is reduced by 30% from nearly 900 to about 600 particles per m^2. This is mainly due to a shift of GAS core position in similar direction for all functions used (see discussion in subsect. **3**˙2). However the estimated N_e is varying within an order of magnitude, leaving discomfort in energy estimation.

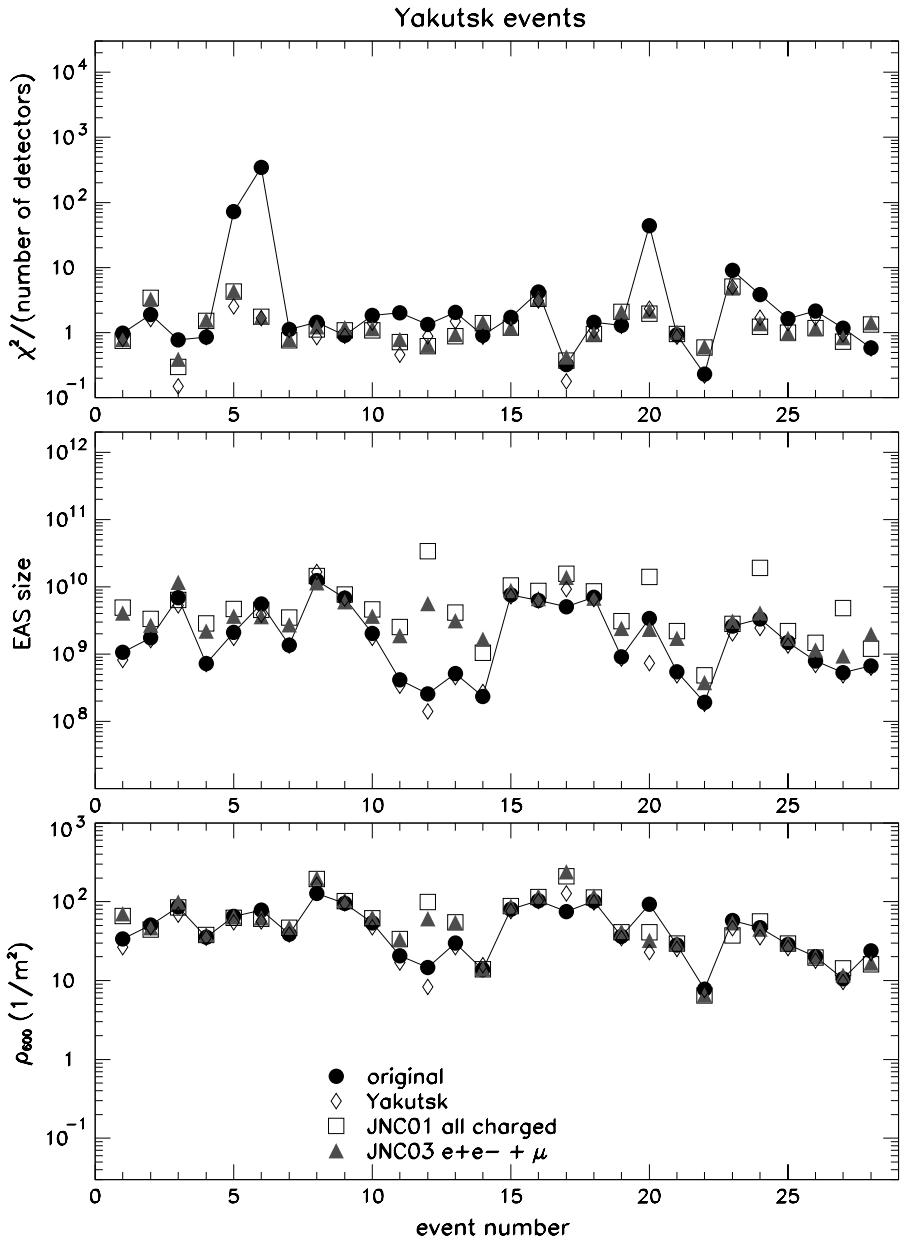

Fig. 10. – Comparison of localization results for Yakutsk data. Original results are compared with fits A, B and C.

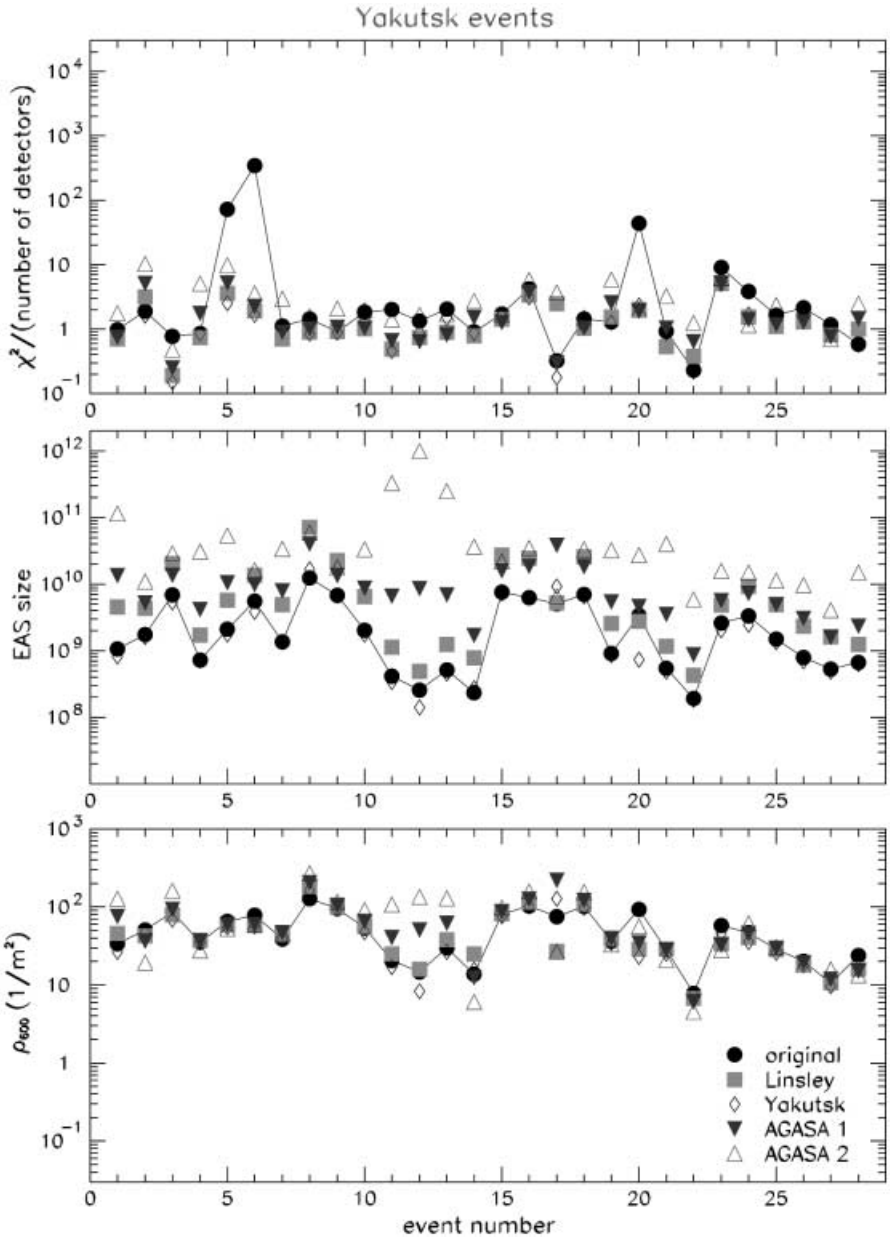

Fig. 11. – Comparison of localization results for Yakutsk data. Original results are compared with fits C, D, E and F.

5. – Conclusions

Although the GAS of energies above 10^{19} eV are being registered near to the maximum of their development the estimation of their energy with accuracy better than 30% is still problematic. We have presented the simplified approach neglecting the fluctuations of size and lateral distribution in individual shower development. The size fluctuations are relatively small near to the depth of the maximum size. The estimation of EAS energy follows the localization procedure which fits the function of lateral distribution of detectable particles to registered densities, to determine the core position, and finally the normalization in terms of $\varrho(600)$ or N_{e}. In most experimental cases detectors are separated by hundreds of meters, whereas the maximum contribution to the total number of particles is in the range 20–200 m, therefore not measured directly. In table I we have shown that the conversion factor $E_0/\varrho(600)$ following from modern simulations can vary within 10% for "perfect" EAS case and $\varrho(600)$ determination. Estimation of N_{e} from $\varrho(600)$ depends on the lateral-distribution function used and is uncertain within 50%.

In the more realistic situation localization procedures are not perfect, mostly due to the low number of detectors hit, and also due to fluctuations in lateral distribution not correctly included in the form of the used function. We noticed that a 60 m error in the core position determination might change normalization up to 40%. It is also worth noticing that the determination of $\varrho(600)$ from data registered in arrays having clusters of more closely separated detectors is more "stable" (*e.g.*, Yakutsk, see figs. 10 and 11) than in $\sim$ 800 m separated detectors (*e.g.*, Volcano Ranch and figs. 8 and 9).

Similarly, there are large discrepancies between localization results when using experimentally derived lateral-distribution functions. The GAS core positions are generally localized within 300 m (between themselves) for Volcano Ranch (*i.e.* large, regular detector separation of about 800 m) or within 60 m for Yakutsk and AGASA events. The axis localization is largely responsible for differences in $\varrho(600)$ estimation in case of Volcano Ranch events. These are much smaller for Yakutsk events. But the estimated sizes (N_{e}) can be different by an order of magnitude (or more) and are due to different shapes of functions at distances smaller than 200 m not covered by experimental measurements.

Sizes of GAS resulting from the lateral-distribution function proposed in this work (JNC01 and JNC03) are generally bigger than sizes obtained from functions derived earlier on the base of experimental data (see figs. 10, 11, 8 and 9). This should be examined in details, especially taking into consideration different energy thresholds of registered particles (we have used 3 MeV threshold for charged electromagnetic component), contribution from energetic photons and contribution from muons. The situation was outlined in fig. 2.

As recently underlined by [28] and [29] the ratio of energy loss of electrons and photons in the scintillator (ϱ_{sc}) to the density of charged particles ($R = \varrho_{\mathrm{sc}}/\varrho_{\mathrm{ch}}$) depends on the distance to the core of GAS. As registrations are taken at large distances the ratio R can be about 1.4. For the primary energy estimations discussed in this paper this would lead to a reduction of the obtained values of ϱ_{600} and N_{e} (and energy) by $\sim$40%. Such circumstance helps a reasonable agreement between ϱ_{600} and sizes from JNC functions in table VI for the most energetic AGASA event.

It is clear for us that further efforts are required for a better understanding of localization procedure and energy estimation. This should obey more realistic simulations of GAS development in the atmosphere and critical comparison with existing data. It would be definitely helpful if the data accumulated over the last several years were available in the Internet network (AGASA and Yakutsk).

Appendix A.

Empirical lateral-distribution functions

A˙1. *AGASA function no. 1*. – This is the function of the form

$$\varrho(r) = N_{\mathrm{e}} \cdot C_{\mathrm{e}} \cdot x^{-\alpha} \cdot (1+x)^{-(\eta-\alpha)} \cdot \left(1 + \frac{r}{2000\ \mathrm{m}}\right)^{-0.5}, \tag{A.1}$$

where $x = r/r_{\mathrm{M}}$, r_{M}—the Molière unit, for Akeno $r_{\mathrm{M}} = 91.6$ m, $\alpha = 1.2$, $\eta = (3.80 \pm 0.05) + (0.10 \pm 0.05) \cdot \log\left(\frac{N}{10^9}\right)$.

This function is plotted in fig. 12 for $\log(N) = 8$, 8.5, 9, 9.5, 10 with $\eta = 3.7$, 3.75, 3.8, 3.85, 3.9,

$$C_{\mathrm{e}} = \frac{\Gamma(\eta-\alpha)}{2\pi \cdot \Gamma(2-\alpha) \cdot \Gamma(\eta-2)} \cdot \frac{1}{r_{\mathrm{M}}^2}.$$

This distribution [30], as underlined by Vishwanath [31] enters in the category of hypergeometric Gaussian functions, like eq. (3) [13], under the general form of the structure function (referred to as JNC function)

$$f(x) = C_j \cdot x^{-\alpha} \cdot (1+x)^{-(\eta-\alpha)} \cdot (1+dx)^{-\beta} \tag{A.2}$$

with the conditions $2-\alpha > 0$ and $\beta + \eta - 2 > 0$.

The value used in eq. (A.1) for the coefficient C_{e} is just an approximation; the exact value is (symbols refer to eq. (A.2))

$$C_j = \frac{\Gamma(\beta+\eta-\alpha)}{2\pi \cdot \Gamma(2-\alpha) \cdot \Gamma(\beta+\eta-2)} \cdot \frac{1}{F_{\mathrm{HG}}(\beta, 2-\alpha, \beta+\eta-\alpha; 1-d)}.$$

The hypergeometric Gaussian function can be easily calculated from the hypergeometric series

$$\begin{aligned} F_{\mathrm{HG}}(a,b,c;z) &= \sum_{n=0}^{\infty} \frac{(a)_n (b)_n}{(c)_n n!} z^n, \qquad c \neq 0, -1, -2, ..., \\ & (a)_n = \Gamma(a+n)/\Gamma(a), \quad (a)_0 = 1. \end{aligned} \tag{A.3}$$

A˙2. *AGASA function no. 2* . – This is a function used in AGASA [27, 32] suitable for inclined showers

$$\varrho(r) = N_{\mathrm{e}} \cdot C_{\mathrm{e}} \cdot x^{-\alpha} \cdot (1+x)^{-(\eta-\alpha)} \cdot \left[1 + \left(\frac{r}{1000\ \mathrm{m}}\right)^2\right]^{-0.6}, \tag{A.4}$$

where $x = r/r_{\mathrm{M}}$, for Akeno $r_{\mathrm{M}} = 91.6$ m, $\alpha = 1.2$, $\eta = 3.97\text{–}1.79 \cdot (\sec\theta - 1)$, with zenith angle θ.

$$C_{\mathrm{e}} = \frac{\Gamma(\eta-\alpha)}{2\pi \cdot \Gamma(2-\alpha) \cdot \Gamma(\eta-2)} \cdot \frac{1}{r_{\mathrm{M}}^2}.$$

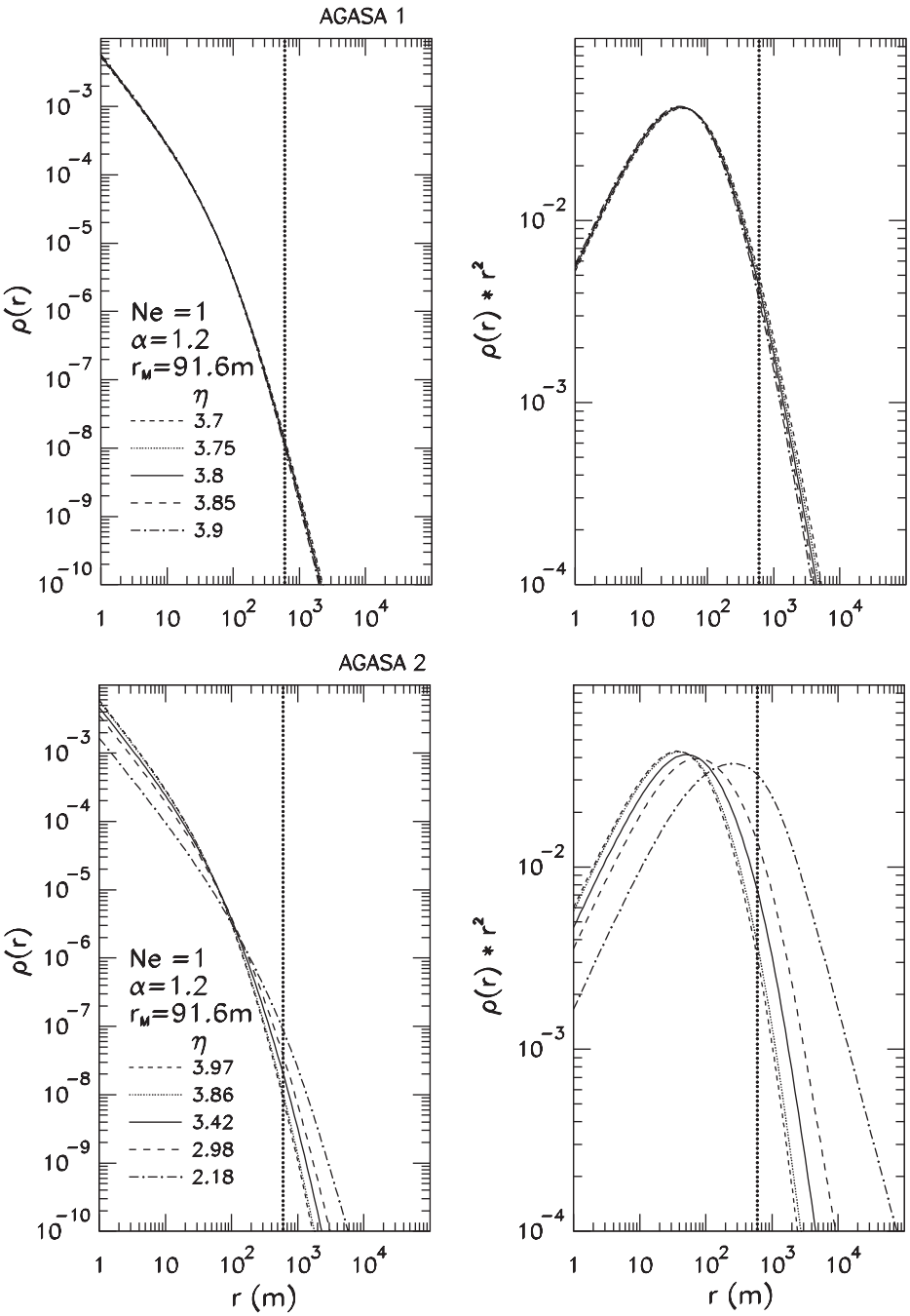

Fig. 12. – Top: distribution of charged particles with AGASA function n°1 (see subsect. A·1). Bottom: AGASA function n°2 (see subsect. A·2). Right panel: respective distributions $r^2 f(r)$, as the total number of particles $N \sim \int r^2 f(r)\ \mathrm{d}(\log(r))$.

However this normalization is not perfect due to the last factor in eq. (A.4) and the additional correction factor $C_{\rm a}$ should be applied:

$$C_{\rm a} = 1 + 6 \cdot \exp\left[\frac{-\sqrt{\eta - 2.07}}{0.218}\right].$$

This (corrected) distribution is represented in fig. 12 for a wider amplitude of parameters than for AGASA no. 1, $\theta = 0°, 20°, 40°, 50°, 60°$, $\eta = 3.97, 3.86, 3.42, 2.98, 2.18$.

A˙3. *AKENO function* . – This function (fig. 13) has the advantage to include the age parameter s and is an extension of relation (2) as the sum of two Euler beta-functions [12]

$$\varrho(r) = N_{\rm e} \cdot C_A \cdot [x \cdot (x+1)]^{s-2} \cdot (x+1)^{-2.5} \cdot (1 + 0.2 \cdot x^{1.3}), \tag{A.5}$$

where $x = r/r_{\rm M}$, $r_{\rm M} = 91.6$ m, $C_A = \dfrac{1}{2\pi \cdot r_{\rm M}^2 \cdot C_0}$, $C_0 = \dfrac{1}{C_1} + \dfrac{1}{C_2}$, $C_1 = \dfrac{\Gamma(4.5 - s)}{\Gamma(s) \cdot \Gamma(4.5 - 2 \cdot s)}$, $C_2 = \dfrac{\Gamma(4.5 - s)}{\Gamma(2.3) \cdot \Gamma(3.2 - 2 \cdot s)}$.

A˙4. *Linsley's function* . – This function [1] enters also in the category of Euler beta-functions, like eq. (2) and takes into account the temperature effect

$$\varrho(r) = N_{\rm e} \cdot C_{\alpha,\eta} \cdot (x)^{-\alpha} \cdot (x+1)^{-(\eta-\alpha)} \cdot \frac{1}{\mathrm{r}_{\rm M}^2}, \tag{A.6}$$

where $x = r/r_{\rm M}$, $r_{\rm M} = 91.6$ m is the Molière unit (generally: $r_{\rm M} = (272.50 \cdot T)/(P - 73.94 \cdot \cos\theta)$, T—the temperature (K), P—the atmospheric pressure at the observation level in mb), θ—the zenith angle, $C_{\alpha,\eta} = \frac{\Gamma(\eta-\alpha)}{2\pi \cdot \Gamma(2-\alpha) \cdot \Gamma(\eta-2)}$, $\eta = b_0 + b_1(\sec\theta - 1) + b_2 \log\left(\frac{N}{10^8}\right)$, $\alpha = \alpha_0 + \alpha_1 \cdot \eta$, $b_0 = 3.70$, $b_1 = -0.57$, $b_2 = 0.085$, $\alpha_0 = -2.135$, $\alpha_1 = 0.948$. This function, originally used for the treatment of the data collected in Volcano Ranch, is plotted in fig. 13.

A˙5. *Yakutsk experimental function* . – This function [23] is based on the scaling properties of the density at 600 m [33]

$$\varrho(r) = C \cdot \varrho_{600} \cdot \frac{600 \text{ m}}{r} \cdot \left(\frac{1 + \frac{r}{r_{\rm M}}}{1 + \frac{600}{r_{\rm M}}}\right)^{1-b}, \tag{A.7}$$

where $b \equiv b(\theta, \varrho_{600}) = (3.54 \pm 0.12) - (2.16 \pm 0.43) \cdot (1 - \cos\theta) + (0.15 \pm 0.05) \cdot \log(\varrho_{600})$, ($b \sim 3.5$–$4$), θ–zenith angle, $r_{\rm M}$ is the Molière unit, $r_{\rm M} = \frac{7.4 \cdot 10^4}{P} \cdot \frac{T}{273}$, T—the temperature (K), P—the atmospheric pressure at observation level in mb, for Yakutsk $r_{\rm M} \approx 68$ m, ϱ_{600} is particle density at the core distance of 600 m, C is the normalization factor and $C = 1$. By integration over the surface $\varrho(r)$ one gets the total number of charged particles N in EAS:

$$N = \int_0^\infty 2\pi \cdot r \cdot \varrho(r)\, \mathrm{d}r = \frac{2\pi r_{\rm M}}{b-2} \, \frac{\varrho_{600} \cdot 600 \text{ m}}{\left(1 + \frac{600 \text{ m}}{r_{\rm M}}\right)^{1-b}}.$$

Both lateral distributions used in Yakutsk for charged particles and muons (eq. (B.5)) are plotted in fig. 14. For the curves in fig. 14: $C = 1/N$.

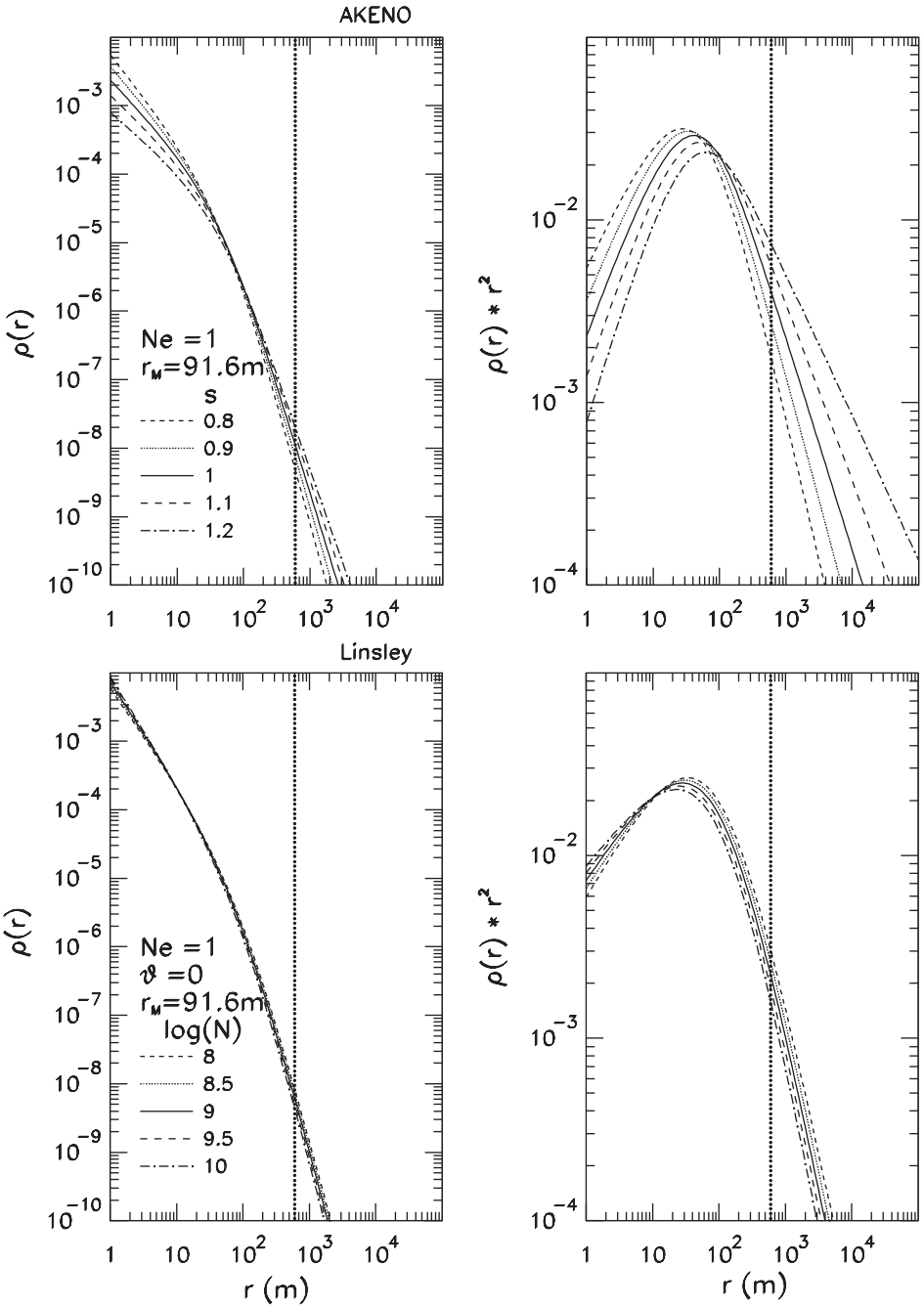

Fig. 13. – Top: Akeno function using age parameter (see subsect. A˙3). Bottom: Linsley's function (see subsect. A˙4).

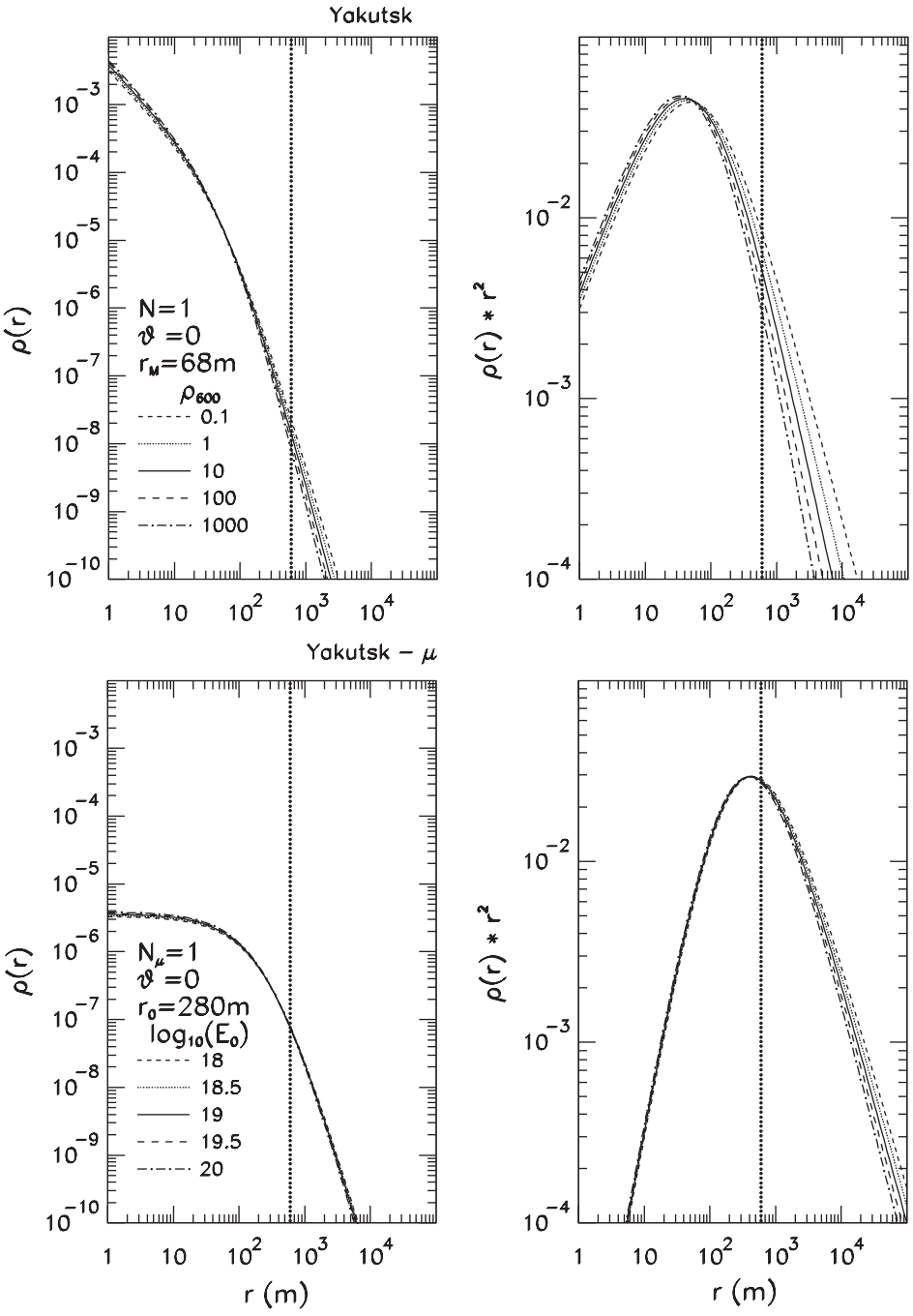

Fig. 14. – Lateral distributions in Yakutsk for charged particles (top) (see subsect. A·5) and muons (bottom) (see eq. (B.5)).

TABLE VII. – *Comparison of results of localization performed for Yakutsk event 7810061014 (see fig. 15) for 4 different lateral-distribution functions. "The principal functions" are written in bold characters.*

Left fig. 15

Function	X_c(m)	Y_c(m)	s	N_e	$\varrho(600)$	χ^2/n
Yakutsk	**1743.8**	−21.0		$\mathbf{1.75{\cdot}10^9}$	**47.5**	**1.43**
AGASA#2				$3.30{\cdot}10^{10}$	90.0	2.29
JNC01			1.15	$4.70{\cdot}10^9$	62.5	1.26
JNC03			1.15	$3.66{\cdot}10^9$	63.8	1.33

Right fig. 15

Function	X_c(m)	Y_c(m)	s	N_e	$\varrho(600)$	χ^2/n
Yakutsk				$1.76{\cdot}10^9$	47.8	1.59
AGASA#2				$3.25{\cdot}10^{10}$	88.6	2.10
JNC01			1.15	$4.65{\cdot}10^9$	61.8	1.10
JNC03	**1719.3**	−0.8	**1.15**	$\mathbf{3.64{\cdot}10^9}$	**63.4**	**1.16**

APPENDIX B.

Empirical lateral-distribution functions for muons

The structure functions for the penetrating component $\phi(x) = \varrho_\mu(r) r_0^2/N_\mu$ (where ϱ_μ and N_μ are, respectively, the density and the muon size, $x = r/r_0$) have been inspired by

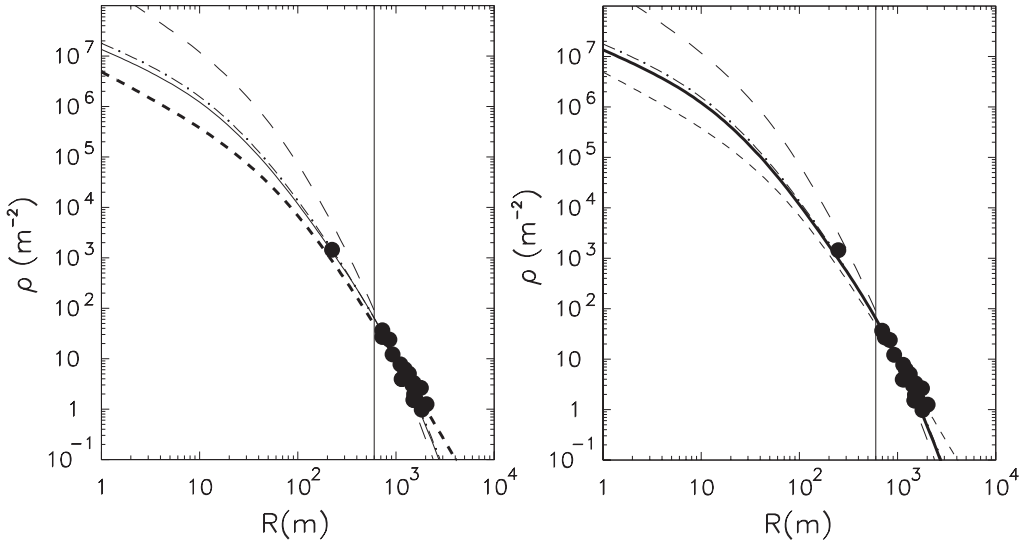

Fig. 15. – Yakutsk event 7810061014. Density distributions for 4 lateral-distribution functions. The short-dashed line represents Yakutsk function, the long-dashed line AGASA#2, the dash-dotted line JNC01 (all charged), and the solid line JNC03 (e^+e^- + muons, $N_\mu/N_e = 0.05$). Vertical line at $R = 600$ m. "Principal functions" are Yakutsk in the left figure and JNC03 in the right one (corresponding lines are thicker). Values of related N_e and $\varrho(600)$ are in table VII.

the transverse-momenta distributions and the geometrical propagation from the initial interactions. Normalized following $\int_0^\infty 2\pi x\phi(x)\,\mathrm{d}x = 1$, they are often presented in two versions, one integrable as the Euler gamma-function and another inspired by the NKG formula, integrable as the Euler beta-function.

They have the forms

$$\phi(r/r_0) = C_\mu (r/r_0)^{-\alpha} \exp[-r/r_0], \qquad C_\mu = \frac{1}{2\pi\Gamma(2-\alpha)} \tag{B.1}$$

$$= C_\mu (r/r_0)^{-\alpha_1} (r/r_0 + 1)^{-\beta_1}, \tag{B.2}$$

$$C_\mu = \frac{\Gamma(\beta_1)}{2\pi\Gamma(2-\alpha_1)\Gamma(\beta_1+\alpha_1-2)}.$$

It is often admitted that those structure functions scale on a large interval of primary energy, but this is an oversimplification, at least for individual showers [34]. Typical values for r_0 for muons above 300 MeV are 180 m and 320 m, respectively, for eqs. (B.1) and (B.2). One general empirical muon lateral function has been formulated also by Greisen [10] as follows:

$$\varrho_\mu(r) = N_\mu \cdot \frac{14.4}{5.84\cdot 10^4} \cdot \left(\frac{51}{E_{\mu\mathrm{th}}+50}\right)^{0.37} \cdot \left(\frac{2.5}{E_{\mu\mathrm{th}}+0.82}\right)^{-0.9} \times \tag{B.3}$$

$$\times\, r^{-3/4} \cdot \left(1+\frac{r}{320\ \mathrm{m}}\right)^{-2.5} \cdot \left(\frac{3}{E_{\mu\mathrm{th}}+2}\right)^{0.14\cdot r^{0.37}},$$

where $E_{\mu\mathrm{th}}$ is the muon energy threshold in GeV. The relation between N_μ and N_e is given by

$$N_\mu(E_\mu > E_{\mu\mathrm{th}}, N_\mathrm{e}) = 5.84\cdot 10^4 \cdot \left(\frac{N_\mathrm{e}}{10^6}\right)^{3/4} \times \tag{B.4}$$

$$\times \left(\frac{51}{E_{\mu\mathrm{th}}+50}\right)^{0.63} \cdot \left(\frac{2.5}{E_{\mu\mathrm{th}}+0.82}\right)^{0.9}.$$

Formula (B.3) can be used for the muon energy region of $0.5\ \mathrm{GeV} < E_{\mu\mathrm{th}} < 50\ \mathrm{GeV}$.

At ultrahigh energy, the structure function of eq. (B.2) is used in Yakutsk [23] in a form suitable for zenith angle dependence:

$$\phi_\mu(r) = C_\mu \cdot K(\theta) \cdot \left(\frac{E_0}{10^{18}\ \mathrm{eV}}\right)^{0.87} \cdot \left(\frac{r}{r_0}\right)^{-0.75} \cdot \left(1+\frac{r}{r_0}\right)^{(0.75-b_\mu)}, \tag{B.5}$$

where $C_\mu = 1$, $r_0 = 280$ m, $K(\theta) = 13.3\cdot\exp\left[(\frac{1}{\cos\theta}-1)\cdot\frac{1020}{440}\right]$, $b_\mu = b_0 + b_1\cos\theta + b_2(\log E_0 - 18)$, $b_0 = 0.98\ \pm 0.03$, $b_1 = 2.28\ \pm 0.3$, $b_2 = 0.09\ \pm 0.01$.

In parallel, for giant EAS, a similar function is used in AGASA with an additive factor for very large distances:

$$\varrho_\mu(r) = N_\mu \frac{C'_\mu}{r_0^2} \left(\frac{r}{r_0}\right)^{-0.75} \left(1+\frac{r}{r_0}\right)^{-\beta} \left[1+\left(\frac{r}{800}\right)^3\right]^{-\delta}, \tag{B.6}$$

where $C'_\mu = 0.325$ for $\beta = 2.52$, $r_0 = 266$ m and $\delta = 0.6$.

TABLE VIII. – *Comparison of results of localization performed for AGASA event #akn25400-0296 (see fig. 16) for 4 different lateral-distribution functions. "The principal functions" are written in bold characters.*

Left fig. 16

Function	X_c(m)	Y_c(m)	s	N_e	$\varrho(600)$	χ^2/n
Yakutsk				$1.57{\cdot}10^{10}$	310.3	9.09
AGASA#2	−1209.7	−1320.1		$\mathbf{9.23{\cdot}10^{10}}$	**632.4**	**5.24**
JNC01			0.91	$1.99{\cdot}10^{11}$	603.1	5.02
JNC03			0.96	$5.04{\cdot}10^{10}$	487.3	5.27

Right fig. 16

Function	X_c(m)	Y_c(m)	s	N_e	$\varrho(600)$	χ^2/n
Yakutsk				$1.59{\cdot}10^{10}$	312.4	8.43
AGASA#2				$8.66{\cdot}10^{10}$	593.1	5.76
JNC01			1.00	$9.60{\cdot}10^{10}$	518.1	5.15
JNC03	−1233.8	−1349.6	**0.95**	$\mathbf{5.05{\cdot}10^{10}}$	**473.5**	**5.03**

APPENDIX C.

Comparison between different lateral-distribution functions and experimental data

C·1. *General remarks.* – The localization procedure for a given event might give different coordinates of the shower core when different lateral-distribution functions were

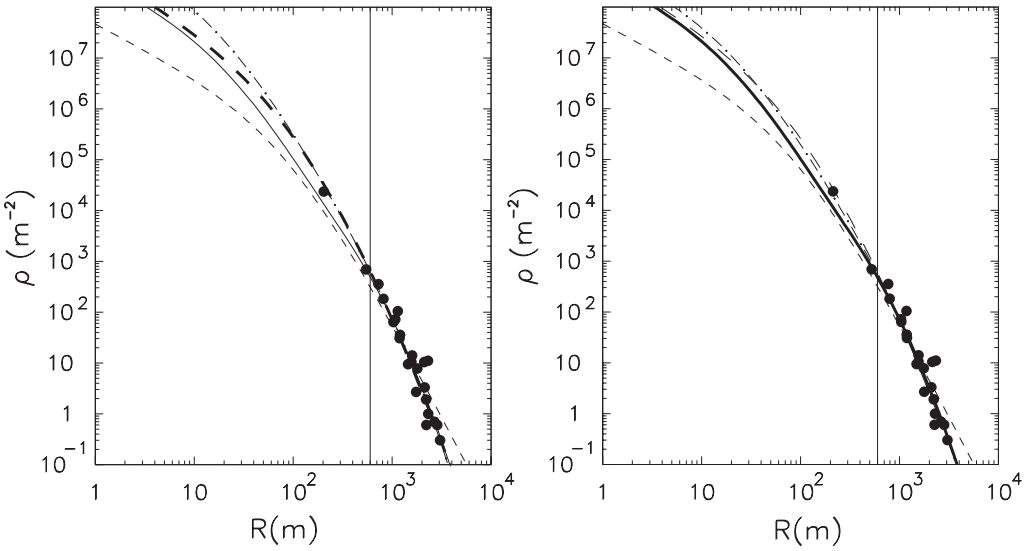

Fig. 16. – AGASA event #akn25400-0296. Density distributions for 4 lateral-distribution functions. Line description as in fig. 15. "Principal functions" are AGASA#2 in the left figure and JNC03 in the right one. See table VIII for a comparison of numerical values.

used. The differences are in most cases within 50 m when the number of hit detectors is greater than 10. To compare different lateral-distribution functions with the data, we use one function (we call it *principal function*) to determine (X_c, Y_c) and the corresponding size (N_e) and $\varrho(600)$ for this function. Then we fit another lateral-distribution function for the already determined (and now fixed) (X_c, Y_c). In this way we can present the difference between shapes of different functions.

C˙2. *Example 1: Yakutsk event 7810061014.* – We compare the Yakutsk event 7810061014 [23] with density distributions for 4 lateral-distribution functions. Two cases are presented in fig. 15 for Yakutsk and JNC03 functions as the *principal functions* for the localization. Some related numerical values are shown in table VII.

C˙3. *Example 2: AGASA event #akn25400-0296.* – For the very large AGASA event #akn25400-0296 [27] density distributions for 4 lateral-distribution functions are presented in fig. 16 and the related numbers in table VIII. *The principal functions* are AGASA#2 and JNC03. It is interesting to compare the values from table VIII with table VI with the best localizations for each function.

REFERENCES

[1] Linsley J., *Catalogue of High Energy Cosmic Rays*, **1** (1980) 3, World Data Center C2, Tokyo, and references herein.
[2] Greisen K., *Phys. Rev. Lett.*, **16** (1966) 748;
[3] Zatsepin G. T. and Kuzmin V. A., *Pis'ma Zh. Exp. Theor. Fiz.*, **4** (1966) 114.
[4] Cronin J. *et al.*, *The Pierre Auger Project*, design report (1995).
[5] Particle Data Group, *Phys. Rev. D*, **54** (1996) 137;
[6] Watson A. A. *et al.*, *Catalogue of High Energy Cosmic Rays*, **1** (1980) 63, World Data Center C2, Tokyo, and references herein;
[7] Sokolsky P., Sommers P. and Dawson B. R., *Phys. Rep.*, **217** (1992) 225.
[8] Williams R. W., *Phys. Rev.*, **74** (1947) 1689.
[9] Kamata K. and Nishimura J., *Suppl. Prog. Theor. Phys.*, **6** (1958) 139.
[10] Greisen K., *Ann. Rev. Nucl. Sci.*, **10** (1960) 63.
[11] Capdevielle J. N. and Gawin J., *J. Phys. G*, **8** (1982) 1317.
[12] Nagano M. *et al.*, *J. Phys. Soc. Jpn.*, **53** (1984) 1667.
[13] Capdevielle J. N. and Procureur J., *Proc. 18th ICRC (Bangalore)*, **11** (1983) 307.
[14] Lagutin A. A., Plyasheshnikov A. V. and Goncharov A. I., *Nucl. Phys. B*, **60** (1998) 161.
[15] Nishimura J., *Hand. Phys.*, **XLVI/2** (1967) 1 (Springer-Verlag).
[16] Bocquet G. *et al.* (UA1 MIMI Collaboration), *Phys. Lett. B*, **366** (1996) 434.
[17] Capdevielle J. N., *Nucl. Phys. B*, **52** (1997) 146.
[18] Capdevielle J. N. *et al.*, The Karlsruhe Extensive Air Shower Simulation Code CORSIKA, KfK report-4998 (KfK Karlsruhe) 1992.
[19] Heck D., Knapp J., Capdevielle J. N., Schatz G. and Thouw T., The CORSIKA Air Shower Simulation Program, FZKA report-6019 (FZK Karlsruhe) 1998.
[20] Le Gall C., Dissertation Ph. Thesis D., University of Paris VII (1999).
[21] Kalmykov N. N., Ostapchenko S. S. and Pavlov A. I., *Nucl. Phys. B*, **52** (1997) 17;
[22] Dai H. Y., Kasahara K., Matsubara Y., Nagano M. and Teshima M., *J. Phys. G.*, **14** (1988) 793.
[23] Efimov N. N., Egorov T. A., Krasilnikov D. D., Pravdin M. I. and Sleptsov Y. E., *Catalogue of High Energy Cosmic Rays*, **3** (1988) 1, World Data Center C2, Tokyo, and references herein.

[24] Efimov N. N., Egorov T. A., Glushkov A. V., Pravdin M. I. and Sleptsov Y. E., *Proc. of the ICRR International Symposium on Astrophysical Aspects of the Most Energetic Cosmic Rays*, edited by Nagano M. and Takahara F. (World Scientific, Singapore) 1991, p. 20.
[25] Winn M. M., Ulrichs J., Peak L. S., McCusker C. B. A. and Horton L., *Catalogue of High Energy Cosmic Rays*, **2** (1986) 3, World Data Center C2, Tokyo, and references herein.
[26] Capdevielle J. N., Le Gall C. and Sanosyan K., *Astropart. Phys.*, **13** (2000) 259.
[27] Yoshida S. *et al.*, *Astropart. Phys.*, **3** (1995) 105.
[28] Kutter T., GAP-98-048 (Auger Technical Note) (1998).
[29] Nagano M., Heck D., Sinozaki K., Inoue N. and Knapp J., *Astropart. Phys.*, **13** (2000) 277.
[30] Nagano M. *et al.*, *J. Phys. G*, **18** (1992) 423;
[31] Vishwanath P. R., *Proc. 23rd ICRC, Rapporteur Papers (Calgary)*, **6** (1993) 384 (World Scientific, Singapore).
[32] Hayashida N. *et al.*, *Phys. Rev. Lett.*, **73** (1994) 3491.
[33] Hillas M., Marsden D. J., Hollows J. D. and Hunter H. W., *Proc. 12th ICRC (Hobart)*, **3** (1971) 1001.
[34] Capdevielle J. N., Gabinski P., Gawin J. and Kouider-Akil A., *J. Phys. G*, **14** (1988) 1537.